Finite element analysis of electrostatic coupled systems using geometrically nonlinear mixed assumed stress finite elements

by

Zhi Cheng Lai

A dissertation submitted in partial fulfilment
of the requirements for the degree of

Master of Engineering

in the Faculty of Engineering, Built Environment and Information Technology,
University of Pretoria

June 2007

Abstract

Title: Finite element analysis of electrostatic coupled systems using geometrically nonlinear mixed assumed stress finite elements

Author: Zhi Cheng Lai

Supervisors: Prof. A.A. Groenwold
Dr. S. Kok

Department: Department of Mechanical and Aeronautical Engineering

Degree: Master of Engineering

Keywords: MEMS, coupled fields, assumed stress, geometrically nonlinear, finite element, Newton's method, analytical gradient

The micro-electromechanical systems (MEMS) industry has grown incredibly fast over the past few years, due to the irresistible character and properties of MEMS. MEMS devices have been widely used in various fields such as aerospace, microelectronics, and the automobile industry. Increasing prominence is given to the development and research of MEMS; this is largely driven by the market requirements.

Multi-physics coupled fields are often present in MEMS. This makes the modeling and analysis of such devices difficult and sometimes costly. The coupling between electrostatic and mechanical fields in MEMS is one of the most common and fundamental phenomena in MEMS; it is this configuration that is studied in this thesis. The following issues are addressed:

1. Due to the complexity in the structural geometry, as well as the difficulty to analyze the behavior in the presence of coupled fields, simple analytical solutions are normally not available for MEMS. The finite element method (FEM) is therefore used to model electrostatic-mechanical coupled MEMS. In this thesis, this avenue is followed.

2. In order to capture the configuration of the system accurately, with relatively little computational effort, a geometric non-linear mixed assumed stress element is developed and used in the FE analyses. It is shown that the developed geometrically non-linear mixed assumed

stress element can produce an accuracy level comparable to that of the Q8 element, while the number of the degrees of freedom is that of the Q4 element.

3. Selected algorithms for solving highly non-linear coupled systems are evaluated. It is concluded that the simple, accurate and quadratic convergent Newton-Raphson algorithm remains best. To reduce the single most frustrating disadvantage of the Newton method, namely the computational cost of constructing the gradients, analytical gradients are evaluated and implemented. It is shown the CPU time is significantly reduced when the analytical gradients are used.

4. Finally, a practical engineering MEMS problem is studied. The developed geometric non-linear mixed element is used to model the structural part of a fixed-fixed beam that experiences large axial stress due to an applied electrostatic force. The Newton method with analytical gradients is used to solve this geometrically nonlinear coupled MEMS problem.

Opsomming

Titel: Eindige element analise van elektrostaties gekoppelde stelsels met behulp van geometries nie-lineêre gemengde eindige elemente gebaseer op aangenome spanningsvelde

Outeur: Zhi Cheng Lai

Studieleiers: Prof. A.A. Groenwold
Dr. S. Kok

Departement: Departement Meganiese en Lugvaartkundige Ingenieurswese

Graad: Magister in Ingenieurswese

Sleutelwoorde: MEMS, gekoppelde velde, aangenome spanning, geometries nie-lineêr, eindige element, Newton se metode, analitiese gradiënt

Die mikro-elektromeganiese sisteem (MEMS) industrie het verbysterend vinnig oor die afgelope paar jaar gegroei, as gevolg van die onweerstaanbare karakter en eienskappe van MEMS. MEMS stelsels word wyd gebruik in verskeie velde soos lugvaart, mikro-elektronika, en die voertuig industrie. Toenemende aandag word aan die ontwikkeling van en navorsing in MEMS geskenk; dit is tot 'n groot mate die gevolg van markverwante aanvraag.

Multi-fisika gekoppelde velde is baie keer aanwesig in MEMS. Dit maak die modelering en analisering van sulke stelsels moeilik, en soms duur. Die koppeling tussen elektrostatiese en meganiese velde in MEMS is een van die mees algemene en fundamentele eienskappe van MEMS; dit is hierdie konfigurasie wat in hierdie tesis bestudeer word. Die volgende punte word aangespreek:

1. As gevolg van geometriese kompleksiteite, asook die moeilikheidsgraad geassosieer met die aanwesigheid van gekoppelde velde, is eenvoudige analitiese oplossings vir MEMS gewoonlik nie beskikbaar nie. Die eindige element metode (EEM) word daarom baie keer gebruik om elektrostaties-meganies gekoppelde MEMS te modelleer. In hierdie tesis word die EEM dan ook gebruik.

2. Ten einde die konfigurasie van die stelsel akkuraat te beskryf, teen 'n relatief lae bereken-

ingskoste, word 'n geometries nie-lineêre aangenome-spanningselement ontwikkel en gebruik in die EE analises. Dit word aangetoon dat die akkuraatheid van die ontwikkelde geometries nie-lineêre aangenome-spanningselement vergelykbaar is met die akkuraatheid van die bekende Q8 element, terwyl die aantal vryheidsgrade natuurlik dieselfde is as vir die bekende, goedkoper Q4 element.

3. Enkele algoritmes vir die oplos van hoogs nie-lineêre gekoppelde stelsels word geevalueer. Dit word dan aangetoon dat die eenvoudige, akkurate en kwadraties konvergente Newton-Raphson algoritme die beste vertoon. Om die mees frustrerende nadeel van die Newton metode, naamlik die berekeningskoste geassosieer met die konstruksie van gradiënte, te oorkom, word analitiese gradiënte geevalueer en geïmplementeer. Dit word aangetoon dat die SVE tye aansienlik verminder indien analitiese gradiënte gebruik word.

4. Laastens word 'n praktiese ingenieurs MEMS probleem bestudeer. Die ontwikkelde geometries nie-lineêre aangenome-spanningselement word gebruik om die strukturele deel van 'n dubbel ingeklemde balk te modelleer, wat hoë aksiale spannings ondervind as gevolg van die aanwending van 'n elektrostatiese kragveld. Die Newton metode met analitiese gradiënte word gebruik om hierdie geometries nie-lineêr gekoppelde MEMS probleem mee op te los.

Acknowledgments

I would like to dedicate this thesis to
my whole family, consanguinity or not.

Half a year after my graduation, July 2003, I have decided to rejoin the academic force and try to tackle the Masters. Professor Groenwold kindly took me in as a member of the structure research family. During the past two and half years time, I have leaned so much from this big family, not only the academic knowledge.

Here, formally I would like to express my sincere gratitude towards the following persons:

- My Supervisor, Professor A. Groenwold, for his invaluable advice and support both on my study and life during those times, without whose guidance I would be lost in so many ways.
- My Co-Supervisor, Dr S. Kok, whose enthusiasm and respect for science have taught me more than his many valued inputs. Also especially thanks for helping me so much with my writing.
- All my friends, especially Dr C. Long, for both academic and social friendship.
- My family, for your ultimate support throughout my life.

Financial support granted by the National Research Foundation of South Africa is gratefully acknowledged.

Contents

List of Figures

List of Tables

Chapter 1

Introduction

1.1 MEMS and its components

Microelectromechanical systems or MEMS are typical components used within a microsystem. A microsystem will typically comprise of components from one or more of three classes: microsensors to detect changes in the system's environment; an intelligent component that makes decisions based on changes detected by the sensors; and microactuators, by which the system can perform necessary actions to change its environment [1].

Currently, the intelligent component of the system would be implemented using microelectronic components; this is a well established technology, and is not discussed in this thesis. Micromechanical devices such as microsensors and microactuators are introduced in the following.

A transducer is a device that converts one physical quantity to another [2]. The deformation of a mechanical structure under an applied electrostatic field is one example. Sensors and actuators are special types of transducers. In this thesis, a microsensor is a device that converts one physical or chemical quantity to an electrical one, for processing by the microsystem [3]. An example being to convert the air temperature to an electrical signal by using a thermo-couple. Similarly, a microactuator is a device which converts an electrical quantity into a physical or chemical one in a microsystem, e.g. the comb-drive actuator invented by Tang [4]. The main parameters useful to describe an actuator are its force and its stroke.

There are various types of microsensors and microactuators distinguished by the physical quantities involved: electrostatic (or electrodynamic), magnetic, piezoelectric, hydraulic, and thermal. Of these, piezoelectric and hydraulic methods currently look promising, but the others also have their place. Electrostatic actuation runs a close third, and is possibly the most common, e.g. comb drives and wobble motors, and is a well developed method. Magnetic actuators usually require relatively high currents (and high power), and on the microscopic scale, electrostatic actuation methods usually offer better output per unit volume (the limit is somewhere in the region of going from 1 cm cubed devices to a few mm cubed - depending on the application) [1]. Thermal actuators also require relatively large amounts of electrical energy, and the heat generated also has to be dissipated. Two MEMS examples are shown in Figure 1.1 and Figure 1.2.

There are different ways to design and analyze MEMS. Accurate modeling using a numerical

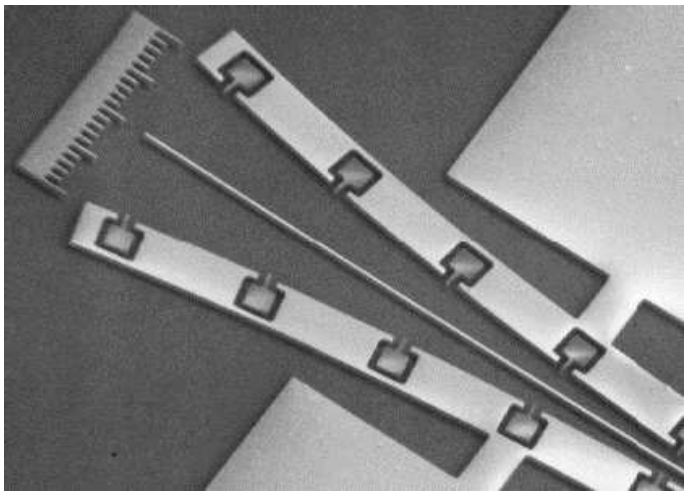

Figure 1.1: SEM photographs of curved electrode actuators showing the entire curved electrode actuator. The thin central beam is movable, being fixed only on it rightmost extreme [5].

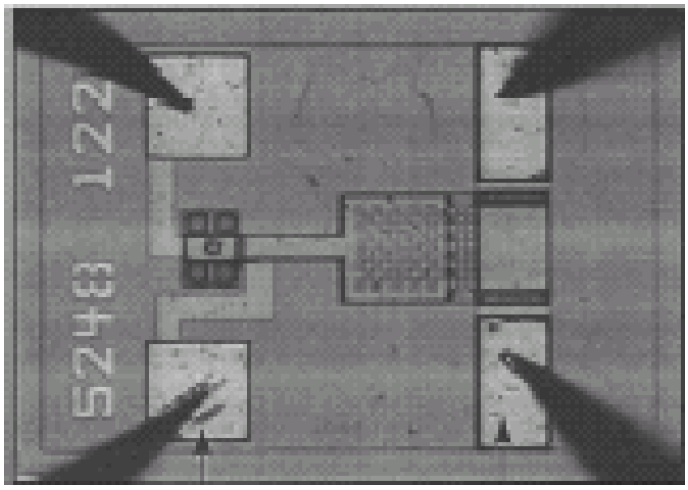

Figure 1.2: Micrograph of the SPST switch developed at Hughes Research Laboratory [6, 7].

method (e.g. FEM or BEM) can be used to solve the partial differential equations that describe a device in different physical domains. These simulation technologies try to give a complete view of the MEMS design, which is material and process dependent, e.g. the nonlinearity that appear in the system. Normally, these nonlinearities arise from two main effects: material nonlinearity, where the relation between the strain and the stress is nonlinear; and geometric nonlinearity, where the material is linear elastic but the relation between force and displacement of an element is nonlinear [8]. The nonlinearities considered in this thesis is restricted to geometric nonlinearities.

1.2 Motivation

The economic significance of MEMS to the world economy is increasing rapidly. A market survey [9] in 2002 predicted that MEMS revenues in the year 2005 may exceed $50 billion [9]. The development of MEMS technology allows us to have better tools to interact with the micro-world. Actually, reduced mass and size allow placing the MEMS in places where a traditional system won't be able to fit [10]. The drive behind the industry is the reduction of the cost, size, and the power consumption of the sensors and actuators, while retaining or improving their performance. Currently, cheap and small MEMS sensors have many applications. Digital cameras for example now use accelerometers to stabilize images, or to automatically find image orientation [11], and accelerometers are also being used in new contact-less game controllers or mice [10].

Model development for electronic components has reached a state of maturity. However, there is a lack of model development for micromechanical devices [12]. Usually, micromechanical devices obey a complex set of equations that must account for the tight coupling of multiple energy domains of the system.

Electrostatic microactuators are widely used in the realization of microsystems [13]. From the design point of view, it is important to obtain an accurate prediction of the behavior of such devices. This means that effective, efficient and robust simulation models are required. Analytical solutions of the coupled electromechanical problem are available only in the case of very simple geometries in small deflection conditions [14]. A more effective approach is the numerical model based, for example, on the finite element method [15].

Large deflections or large axial stresses can arise in the electrostatic microactuators, which will introduce geometrical non-linearity, in addition to the non-linearities that characterize the electromechanical coupling. This could significantly increase the computational complexity of the problem.

It is the aim of this study to review, investigate and modify the entire procedure of analyzing the electromechanical coupled system including element analysis, FEM modeling and algorithm evaluation.

1.3 Objectives

The four objectives of this study are

1. to develop a geometrically nonlinear mixed assumed stress element,
2. to model electrostatic-mechanical coupled fields,
3. to solve the modeled non-linear systems, and
4. to apply the modified element and algorithm to an engineering problem.

1.4 Thesis overview

The Chapters in this thesis are self-contained; each chapter has its own objective.

In Chapter 2, the basic governing equations involved in the multiphysics modeling are introduced. In particular, the formulations involved in electro-mechanical coupled systems are examined. In addition, a brief background and history of the development of MEMS is introduced.

In Chapter 3, a geometrically nonlinear mixed assumed stress element is derived. This element is developed based on the linear 5β hybrid element. This chapter commences with the formulation of a linear mixed assumed stress element. Then, the fundamental differences between linear and geometrically nonlinear formulations are discussed in detail. With the strong form being developed, the finite element formulation for the geometrically nonlinear mixed assumed stress element is proposed. With the patch test, the element is proved to be consistent. Additionally, with a few commonly known numerical benchmark tests, the proposed element is proven to be computational efficient and accuracy comparable.

In Chapter 4, electrostatic-mechanical coupled MEMS are studied. Due to the complexity of the problem, FEM is used to model the coupled system. In order to solve the nonlinear coupled system efficiently with Newton's method, analytical gradients are derived so that the computational cost in calculating the Newton's step is significantly reduced. Besides Newton's method with analytical gradients, other methods for solving nonlinear systems are also introduced in comparison with the proposed one. A few numerical results shows that Newton's method with analytical gradients is an efficient and accurate method to solve the electromechanical coupled system. Finally, the geometrically nonlinear mixed assumed stress element developed in the previous Chapter is used to model a geometrically nonlinear MEMS which is solved using the proposed method.

In Chapter 5, conclusions and recommendations are offered.

In the Appendices, intricate mathematical formulations that may distract from reading the main chapters, are presented.

Chapter 2

Formulation and background

2.1 Formulation of multiphysics (coupled-field modeling)

MEMS devices are mostly multiphysics coupled devices. The physical quantities involved in MEMS may include electrostatic, magnetic, piezoelectric, hydraulic, thermal, and mechanical effects, etc.

Some of the frequently attributed meanings of the term multiphysics are: "multifield" to denote the simultaneous excitation and response of the system by multiple physical fields and; "multidomain" to denote the interaction among continuum representations of systems with drastically different properties (e.g. fluid- structure interaction, moving solidification boundary problems, etc.) through sharable boundaries.

A general formulation of a mathematical model describing the behavior of multiple interacting continua under multifield conditions at a given length scale can be presented as the following system of generally coupled equations

$$\Im_{di}(\hat{m}_{dj}, \hat{n}_{dj}; \dot{m}_{dj}, \dot{n}_{dj}) = \mathbf{0} \quad \text{in} \ \ \Omega_d \tag{2.1}$$

where i, j and d are the number of equations, the number of conjugate field pairs and the number of domains respectively [16]. The operator $\Im_{di}$ (usually differential) expresses some conservation law and is defined per equation per domain while it represents the nature of the behavior of the system as defined by conjugate state variable pairs $(\hat{m}_{dj}, \hat{n}_{dj})$ and for some cases their time derivatives $(\dot{m}_{dj}, \dot{n}_{dj})$. Since the presence of the differential operator $\Im_{di}$ in (2.1), it is usually difficult, if possible, to get the direct analytical solutions. Therefore move advanced numerical methods such as the finite element method are normally deployed in solving (2.1).

2.2 Electrostatic-mechanical coupled field

The key component of many modern MEMS is the simple idealized electrostatic device. In fact, a scale effect is the reason why electrostatic forces, normally negligible at macroscopic level, can prevail over other kinds of actuation (i.e. electromagnetic, piezoelectric) at the microscopic scale

[17]. The electrostatic actuation uses the nature of electrostatic force provided by parallel plate capacitor structures or comb-finger structures. The attractive and repulsive forces generated by electric charge distribution are used to convert electrical to mechanical energy. The electrostatic actuated devices (e.g., micromirror array, microswitch, scanner, microshutter, micromotor) are widely used in varieties of fields. In Figure 2.1 different types of electrostatic actuators are shown [10].

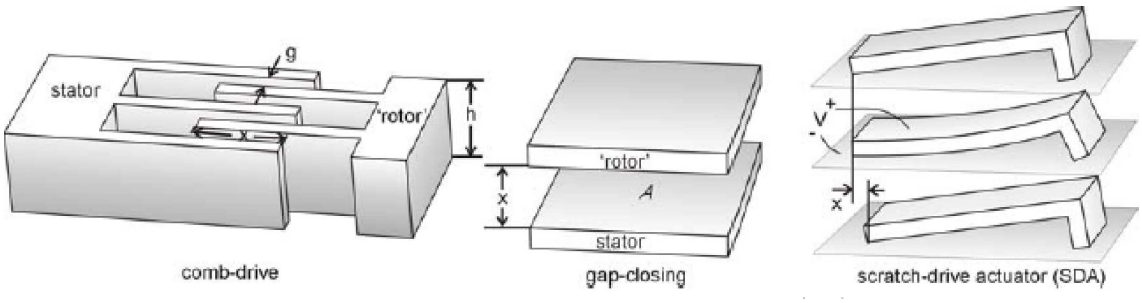

Figure 2.1: Different types of electrostatic actuators

When designing electro-mechanical actuators one typically applies a voltage to the undeformed device. This induces charges on the surface of the conductors in the problem, and those charges induce surface normal pressures over the device. We refer to these pressures as the electrostatic load. The electrostatic load causes the device to deform. In general such deformation will lead to reorganization of all surface charges (and thus pressures) on the device.

The simplicity and importance of this technique have inspired numerous researchers to study mathematical models of electrostatic-elastic interactions. The mathematical analysis of these systems started in the late 1960s with the pioneering work of H. C. Nathanson and his coworkers [18] who constructed and analyzed a mass-spring model of electrostatic actuation, and offered the first theoretical explanation of pull-in instability.

Pull-in phenomenon is a discontinuity related to the interplay of the elastic and electrostatic forces [19]. The pull-in instability in electrostatically actuated MEMS presents a ubiquitous challenge in MEMS technology of great importance. The determination of the pull-in voltage and position requires the solution of a coupled electrostatic-elastic system [20]. In this instability, when applied voltages are increased beyond a critical value, there is no longer a steady-state configuration of the device where mechanical members remain separate, i.e. the structure stiffness can no longer balance the electrostatic force so that the structure just simply 'collapses'.

Another issue associated with the analysis of MEMS is that a linear model is unsuitable for simulation of devices where the deflection is large or where large axial stress exists in the structure. Geometrically nonlinear analysis is needed to model and analyze the system accurately. However the geometric non-linearities induced in addition to the non-linearities that characterize the electromechanical coupling can increase the computational complexity of the problem [21].

For steady state (or quasi-static) electro-mechanical analysis, there are two main governing equations involved when solving the coupled fields. These are force equilibrium form continuum me-

chanical analysis and Gauss's law of electrostatics. These governing equations are expressed as

$$\nabla \cdot (O(\nabla \boldsymbol{u}(\boldsymbol{x}))) = \mathbf{0} \quad \text{in } \Omega_s \tag{2.2}$$

$$\nabla \cdot (\nabla(V)) = \mathbf{0} \quad \text{in } \Omega_e \tag{2.3}$$

where $\boldsymbol{x}$ is a point on the initial structure; $\boldsymbol{u}(\boldsymbol{x})$ is the displacement of that point from its initial position; O is the nonlinear algebraic operator which relates the displacement gradient to the material stresses; V is the scalar voltage; Ω_s is the interior of the structure and Ω_e is the interior of the electrical field. The solution to the above governing equations must also satisfy the prescribed boundary conditions, e.g. prescribed displacements, tractions, voltages or charge densities.

Due to the difficulty of solving the governing equations (2.2) and (2.3) directly, the steady-state electrostatic-mechanical problem can be discretized using the finite element method. The coupled system is described by a three-field formulation, where the structure is modeled by a finite element model and the electrostatic pressure is predicted by a finite element discretization of the electrostatic field. A third field is introduced to describe the motion of the electrostatic mesh. In this way, the structured electrostatic mesh generation can be done relatively easy. The advantages of this approach have been illustrated in the context of aeroelasticity [22] and design optimization of aeroelastic structures [23, 24].

2.3 Brief background of MEMS

Interest in the micromechanical world began in 1959, when Richard Feynman's idea of operation at the micro scale was partially realized with the introduction of silicon transistors and integrated circuits (better known as microchips). Although microchips were developed in the 1970s, research on micromechanical devices did not begin in earnest until the late 1980s, when fabrication techniques used to make microchips were applied to making mechanical structures [25].

In the late 1980s, silicon very-large-scale-integrated (VLSI) design and manufacturing was developed for use in the field of MEMS [26]. Because micromechanics began with techniques used in microchip manufacture, researchers used silicon and other microchip materials. Silicon devices still dominate the MEMS arena because of extensive experience with its fabrication, but research into using other materials such as glass and plastic has produced alternatives to silicon MEMS.

In the 1990s, much research has been done on micromachining. It was said to be the decade of micromachining. Various manufacture and fabrication techniques such as Excimer laser and LIGA [27] were developed to match the fast growing market of the MEMS. Micromachining has become one of the constructional technologies of microengineering alongside microelectronics.

Miniaturization is often a most important driver behind MEMS development. The common perception is that miniaturization reduces cost, by decreasing material consumption and allowing batch fabrication, but an important collateral benefit is also in the increase of applicability [10]. The miniaturization of nearly all other types of devices and systems is arguably an even greater opportunity for commercial profit and beneficial technological advances [28]. However, instead of the traditional evolutionary engineering effort to reduce size and power while simultaneously increasing the performance of such a diverse set of systems, the field of MEMS represents an

effort to radically transform the scale, performance and cost of these systems by employing batch-fabrication techniques and the economies of scale successfully exploited by the integrated circuit (IC) industry [29].

Due to the enormous breadth and diversity of the devices and systems that are being miniaturized, the acronym MEMS, introduced by Howe in 1989 [30], is not a particularly apt one (i.e., the field is more than simply micro, electrical and mechanical systems). However, MEMS is used almost universally to refer to the entire field [31]. Other names for this general field of miniaturization include microsystems technology (MST), popular in Europe, and micromachines, popular in Asia.

Chapter 3

Geometrically nonlinear mixed assumed stress element

In order to capture the geometrically nonlinear effect that may arise in the simulation of MEMS accurately and efficiently, a new geometrically nonlinear mixed assumed stress element is developed in this chapter, similar to the well-known linear 5β element of Pian and Sumihara [32]. Similar elements have been developed before, but the element presented here is particularly simple in its formulation.

Here, a weighted-residual approach is used to formulate the element, since this easily relates to the now well-known Tonti-diagrams.

A variational formulation is presented in References [33, 34]. The approach followed in this chapter is simple, and is developed from first principles. Seemingly, it is easier understood and implemented than the previous formulations. For the sake of numerical simplicity, only a 2-D plane model is considered. The shell and solid versions of this element can be development in a similar way as done for the 2-D shell; related references are References [35, 36]. Another comparable element is the so-called superconvergent element proposed by Liu, Belytschko and Chen [37]. However, this element is inherently rank deficient, and also depends on a stabilization procedure. The development herein was done independent of previous contributions.

3.1 Introduction

In linear elastostatics, membrane finite elements based on the Hellinger-Reissner two field principle have for some time been an alternative to single field displacement based elements, derived from the principle of potential energy.

On the one hand, the simple displacement based Q4 element, based on bilinear displacement interpolation functions, is notoriously inaccurate in bending dominated problems. On the other hand, mixed elements, based on independent stress and displacement interpolations, perform very well in bending dominated situations. A typical example being the 5β two field element proposed by Pian and Sumihara [32]. This element is arguably the most popular two field element available in commercial finite element programs today.

Most certainly, higher order displacement based elements are viable alternatives to two field mixed elements in bending dominated problems; the most popular example of such an element is probably the well-known Q8 serendipity element, which is based on bi-quadratic displacement interpolation functions. However, while an increase in polynomial interpolation order in displacement based elements has certain advantages over low order elements based on two field principles, there are also disadvantages. Advantages of Q8 over 5β for example include the conceptual simplicity of the Q8 element, and the fact that no local element inversions are required.

Disadvantages of Q8, when compared to 5β, include the very fact that additional nodes are carried per element (although this can also be a modeling advantage). Low order elements allow for reduced connectivity in the assembled structural stiffness matrix, which may have definite advantages during solution of the structural system when the system becomes (very) large.

In addition, on the basis of number of elements in a given mesh, Q8 may of course be expected to yield more accurate results than 5β. However, on the basis of number of degrees of freedom in a given mesh, this is not necessarily true.

Low order elements seem very attractive in iterative procedures like optimal structural design. In topology optimization for example, a cursory glance at the literature suffices to reveal that the use of low order Q4 elements by far exceeds the use of higher order elements. This notwithstanding the fact that the low order Q4 element is susceptible to the highly undesirable locking-like phenomena known as 'checkerboarding', from which the Q8 element does not suffer mostly. The fact that the Q4 element requires heuristics to overcome checkerboarding does not in the least reduce its popularity in topology optimization.

Furthermore, the Q8 element is inherently quite stiff; reduced integration is normally used to alleviate this. Reduced integration however results in the introduction of a spurious mode or mechanism on the element level. While this mechanism is in general, and fortuitously, non-communicable in any assembly of two or more elements, it is possible to demonstrate situations where the mechanism does propagate [38]. Notorious examples include vibration analysis, even for over-constrained structures.

Convergence rate considerations are probably also important when selecting elements. The convergence rate of the quadratically interpolated Q8 element is of course superior to the convergence rate of the assumed stress 5β element (being cubic versus quadratic). This seems an enticing argument indeed for using Q8 elements. However, in many practical analysis, singularities are an inevitable part of the problem description. In the presence of singularities, the severity of the singularities greatly influence the demonstrated overall convergence rate; largely, the convergence rates of all elements are equal in the presence of singularities. Phenomena which induce singularities into a model include mesh related discontinuities like sharp re-entrant corners, and discontinuities in the description of boundaries and applied tractions.

However, notwithstanding the foregoing remarks, it will probably remain an open question whether (relatively accurate) low order elements are preferable to higher order elements, and *vice versa*. In part, selection of a given element by the analyst will depend on the capabilities and limitations of in-house supportive software, e.g. mesh generators. One also has to acknowledge that element selection often depends on the the personal preference of the analyst.

Hence, if there are any certainties regarding the relative virtues of different element formulations, it is that the availability of a number of analysis options (elements) seems attractive indeed. It is

for this very reason that we concern ourselves with the advanced low order element for geometric nonlinear analysis presented in the following sections.

Many a low order geometric nonlinear element is intended for inclusion in explicit finite element analysis codes. In these codes, explicit time integration steps are used. The single most important aspect is computational efficiency, since very large finite element meshes are often required. A typical example being crash analysis. In explicit finite element codes, the emphasis on computational efficiency makes reduced integration of simple, displacement based elements an attractive feature. The resultant analysis can of course become unstable, often only controlled by highly skilled and experienced developers and users of these codes. Sometimes, stabilization schemes are used, but these do not guarantee unconditional stability. Nevertheless, reduced integration is a necessity in explicit simulation codes.

In this work, we focus on rank sufficient geometric nonlinear formulations; the intended application being implicit finite element analysis codes. Hence a mixed formulation is attractive, in particular if low order elements are desirable, and if bending dominated problems are studied.

The element proposed herein is an extension of the popular linear elastostatic 5β formulation proposed by Pian and Sumihara, since we opt for the same stress interpolation matrix. (Many other possibilities exist.) The extended formulation provides for geometric nonlinearity; four numerical example problems are presented. In the next chapter, the application of the element proposed herein to very slender nonlinear electrostatic MEMS devices is demonstrated. In this application, Q4 elements proved to be so stiff, that sufficient accuracy could not be attained with reasonable meshes.

This chapter is constructed as follows: In Section 3.2, we recap the formulation of the linear elastic assumed stress mixed formulation. However, rather than starting with the Hellinger-Reissner two field principle, we choose to depart from equilibrium, merely because this simplifies the presentation of the nonlinear formulation. In Section 3.3 we then present our geometrically nonlinear assumed stress formulation. In both Section 3.2 and Section 3.3, we present applicable Tonti diagrams for illustrative purposes. Numerical results are presented in Section 3.4, and concluding remarks are offered in Section 3.5. For the sake of completeness, intricate element operators are presented in Appendix A, where their presentation does not distract from reading the Chapter.

3.2 Linear elastic assumed stress mixed formulation

We will now briefly review the formulation of the linear elastic assumed stress mixed element. Let $\bar{\Omega}$ be the closed and bounded domain occupied by a solid body. The interior part of $\bar{\Omega}$ is denoted Ω and it's boundary $\partial\Omega = \Gamma$, i.e. $\bar{\Omega} = \Omega \cup \partial\Omega$. The boundary consists of that part where surface tractions $\bar{\boldsymbol{t}}$ are prescribed (Γ_t) and a part where displacements $\bar{\boldsymbol{u}}$ are prescribed (Γ_u), with $\Gamma = \Gamma_u \cup \Gamma_t$. In the domain Ω, the strong form of the linear elastic boundary value problem is given by [39]

$$\mathrm{div}\boldsymbol{\sigma} + \boldsymbol{f} = \boldsymbol{0}, \tag{3.1}$$

$$\boldsymbol{\sigma} = \boldsymbol{\mathcal{C}}\boldsymbol{\varepsilon}, \tag{3.2}$$

$$\boldsymbol{\varepsilon} = \frac{1}{2}(\nabla\boldsymbol{u} + \nabla\boldsymbol{u}^{\mathrm{T}}), \tag{3.3}$$

and on the boundary Γ,

$$\boldsymbol{\sigma n} = \bar{\boldsymbol{t}} \quad \text{on} \quad \Gamma_t, \tag{3.4}$$

$$\boldsymbol{u} = \bar{\boldsymbol{u}} \quad \text{on} \quad \Gamma_u, \tag{3.5}$$

where $\boldsymbol{u}$ is the displacement field, $\boldsymbol{\varepsilon}$ is the infinitesimal strain tensor, $\boldsymbol{\sigma}$ is the stress tensor, $\boldsymbol{f}$ is the body force vector, $\boldsymbol{\mathcal{C}}$ is the fourth order tensor that contains the elastic constants of the generalized Hooke's law, $\bar{\boldsymbol{t}}$ is the prescribed traction on the boundary Γ_t with outward unit normal $\boldsymbol{n}$ and $\bar{\boldsymbol{u}}$ is the prescribed displacement on the boundary Γ_u.

In the assumed-stress mixed formulation, we solve for two *independent* fields, namely displacement $\boldsymbol{u}$ and stress $\boldsymbol{\sigma}$. The Tonti diagram [40] in Figure 3.1 depicts this formulation, where the filled boxes are used to indicate the primary fields. Derived quantities (or slave fields) are indicated by dashed boxes, and subscripts are used to indicate to which primary field the slave field is related, e.g. $\boldsymbol{\varepsilon}_u$ is the strain field computed from the displacement, whereas $\boldsymbol{\varepsilon}_\sigma$ is the strain field computed from the stress field. Strong enforcement of relationships is indicated by a double line, whereas weak enforcement of relationships is indicated by a single line.

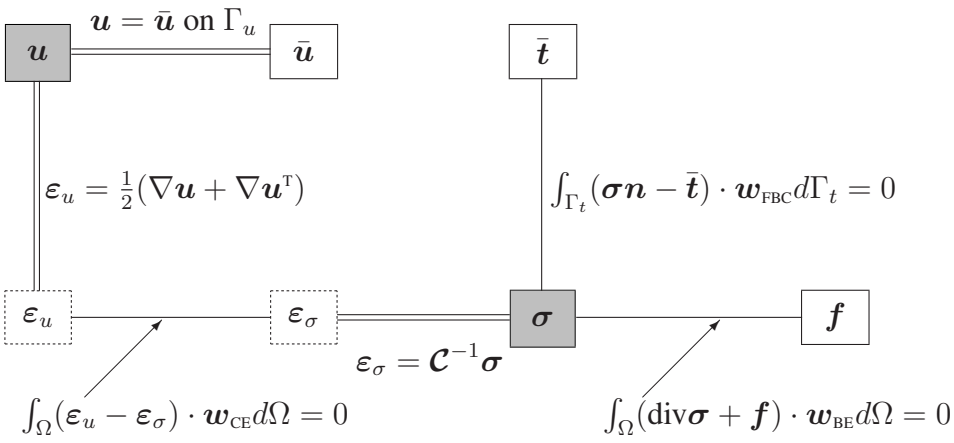

Figure 3.1: Tonti-diagram of linear elastic assumed stress mixed formulation.

In the displacement based formulation, only the equilibrium equation (3.1) and the traction boundary condition (3.4) are enforced in a weak sense. However, in the mixed formulation the stress field is independently interpolated. This stress field is solved by equating the two strain fields $\boldsymbol{\varepsilon}_u$ and $\boldsymbol{\varepsilon}_\sigma$ in a weak sense. Hence, the weak formulation of the linear elastic boundary value problem is given by

$$\int_\Omega (\mathrm{div}\boldsymbol{\sigma} + \boldsymbol{f}) \cdot \boldsymbol{w}_{\mathrm{BE}} d\Omega = 0, \tag{3.6}$$

$$\int_\Omega (\boldsymbol{\varepsilon}_u - \boldsymbol{\varepsilon}_\sigma) \cdot \boldsymbol{w}_{\mathrm{CE}} d\Omega = 0, \tag{3.7}$$

where $\boldsymbol{w}_{\mathrm{BE}}$ is an arbitrary weighting function on the balance (equilibrium) equation, with $\boldsymbol{w}_{\mathrm{BE}} = \boldsymbol{0}$ on Γ_u, and $\boldsymbol{w}_{\mathrm{CE}}$ is an arbitrary weighting function on the compatibility equation. Applying the

divergence theorem to (3.6), and enforcing the traction boundary condition in a weak sense, we obtain

$$\int_{\Omega}(-\boldsymbol{\sigma}\cdot\nabla\boldsymbol{w}_{\text{BE}}+\boldsymbol{f}\cdot\boldsymbol{w}_{\text{BE}})d\Omega+\int_{\Gamma}\bar{\boldsymbol{t}}\cdot\boldsymbol{w}_{\text{BE}}d\Gamma=0. \tag{3.8}$$

3.2.1 Finite element formulation

Henceforth, we will use square brackets [ ] to indicate matrices, and curly braces { } to indicate vectors. The displacement field is interpolated as

$$\boldsymbol{u}=\sum_{e}\boldsymbol{u}^{\boldsymbol{e}}=\sum_{e}[N^e]\{U^e\}, \tag{3.9}$$

where the matrix $[N^e]$ contains elemental nodal interpolation functions, and the vector $\{U^e\}$ contains elemental nodal displacements. For the sake of notational brevity, elemental superscripts 'e' and summation over the elements are henceforth neglected, but are implied. Using this simplified notation, (3.9) for example becomes

$$\boldsymbol{u}=[N]\{U\}. \tag{3.10}$$

Now, following the usual Bubnov-Galerkin approach, the weighting function $\boldsymbol{w}_{\text{BE}}$ is interpolated using the same interpolation functions as those used for displacement, hence

$$\boldsymbol{w}_{\text{BE}}=[N]\{W_{\text{BE}}\}, \tag{3.11}$$

with $\{W_{\text{BE}}\}$ a vector containing the nodal weighting values. The gradient of the weighting functions follows as

$$\nabla\boldsymbol{w}_{\text{BE}}=[B]\{W_{\text{BE}}\}, \tag{3.12}$$

where the matrix $[B]$ contains the spatial gradients of the interpolation functions $[N]$.

The element stress field $\boldsymbol{\sigma}$ is interpolated as

$$\boldsymbol{\sigma}=[P]\{\beta\}, \tag{3.13}$$

with $[P]$ the stress interpolation matrix, in turn expressed in terms of the elemental stress parameter vector $\{\beta\}$. This stress interpolation is continuous within an element, but inter-element discontinuities are allowed.

Substituting (3.12) and (3.13) into (3.8), we obtain

$$\int_{\Omega}\{W_{\text{BE}}\}^{\text{T}}\left(-[B]^{\text{T}}[P]\{\beta\}+[N]^{\text{T}}\{f\}\right)d\Omega+\int_{\Gamma}\{W_{\text{BE}}\}^{\text{T}}[N]^{\text{T}}\{\bar{t}\}d\Gamma=0. \tag{3.14}$$

Since the vector $\{W_{\text{BE}}\}$ contains nodal values, it is removed from the integrals. Furthermore, since the nodal values in $\{W_{\text{BE}}\}$ are arbitrary, it follows that

$$\int_{\Omega}[B]^{\text{T}}[P]\{\beta\}d\Omega=\int_{\Omega}[N]^{\text{T}}\{f\}d\Omega+\int_{\Gamma}[N]^{\text{T}}\{\bar{t}\}d\Gamma. \tag{3.15}$$

The stress interpolation parameters in $\{\beta\}$ are eventually obtained via (3.7). The strain derived from the displacement field is given by

$$\boldsymbol{\varepsilon}_u = [B]\{U\}, \tag{3.16}$$

whereas the strain derived from the stress field is given by

$$\boldsymbol{\varepsilon}_\sigma = [\mathcal{C}]^{-1}\{\sigma\} = [\mathcal{C}]^{-1}[P]\{\beta\}. \tag{3.17}$$

Selecting the Bubnov-Galerkin method again prescribes that the weighting functions $\boldsymbol{w}_{\text{CE}}$ are interpolated using the same interpolation matrix $[P]$ as used for stresses, hence

$$\boldsymbol{w}_{\text{CE}} = [P]\{W_{\text{CE}}\}. \tag{3.18}$$

Substituting (3.16) through (3.18) into (3.7), we obtain

$$\int_\Omega \{W_{\text{CE}}\}^{\text{T}}[P]^{\text{T}}\left([B]\{U\} - [\mathcal{C}]^{-1}[P]\{\beta\}\right) d\Omega = 0. \tag{3.19}$$

Again, since $\{W_{\text{CE}}\}$ contains arbitrary nodal quantities it can be removed from the integral, and we obtain

$$\left(\int_\Omega [P]^{\text{T}}[B]d\Omega\right)\{U\} = \left(\int_\Omega [P]^{\text{T}}[\mathcal{C}]^{-1}[P]d\Omega\right)\{\beta\}. \tag{3.20}$$

The stress interpolation parameters in $\{\beta\}$ are solved from (3.20):

$$\{\beta\} = \left(\int_\Omega [P]^{\text{T}}[\mathcal{C}]^{-1}[P]d\Omega\right)^{-1}\left(\int_\Omega [P]^{\text{T}}[B]d\Omega\right)\{U\}. \tag{3.21}$$

The formulation is completed by substituting (3.21) into (3.15) to obtain the linear system of equations

$$[K]\{U\} = \{\mathcal{F}\}. \tag{3.22}$$

The global stiffness matrix $[K]$ and global load vector $\{\mathcal{F}\}$ are computed from

$$[K] = \sum_e \left(\int_\Omega [B]^{\text{T}}[P]d\Omega_e\right)\left(\int_\Omega [P]^{\text{T}}[\mathcal{C}]^{-1}[P]d\Omega_e\right)^{-1}\left(\int_\Omega [P]^{\text{T}}[B]d\Omega_e\right), \tag{3.23}$$

and

$$\{\mathcal{F}\} = \sum_e \left(\int_\Omega [N]^{\text{T}}\{f\}d\Omega_e + \int_\Gamma [N]^{\text{T}}\{\bar{t}\}d\Gamma_e\right), \tag{3.24}$$

where we now explicitly indicate summation over elements e. It follows from (3.23) that the stiffness matrix is symmetric.

3.3 Geometrically nonlinear assumed stress mixed formulation

Let us now review the geometrically nonlinear formulation of the solid mechanics boundary value problem. Consider the deformable body depicted in Figure 3.2. Due to the possible presence or large displacements and/or rotations, it now becomes necessary to distinguish between the undeformed and deformed bodies. The undeformed body is denoted by $\mathcal{B}_o$, whereas the deformed body is denoted by $\mathcal{B}$. Again, let $\bar{\Omega}$ be the closed and bounded domain occupied by the deformed solid body $\mathcal{B}$. The interior part of $\bar{\Omega}$ is denoted Ω and it's boundary Γ, i.e. $\bar{\Omega} = \Omega \cup \Gamma$. The boundary consists of that part where surface tractions $\bar{\boldsymbol{t}}$ are prescribed (Γ_t) and a part where displacements $\bar{\boldsymbol{u}}$ are prescribed (Γ_u), with $\Gamma = \Gamma_u \cup \Gamma_t$.

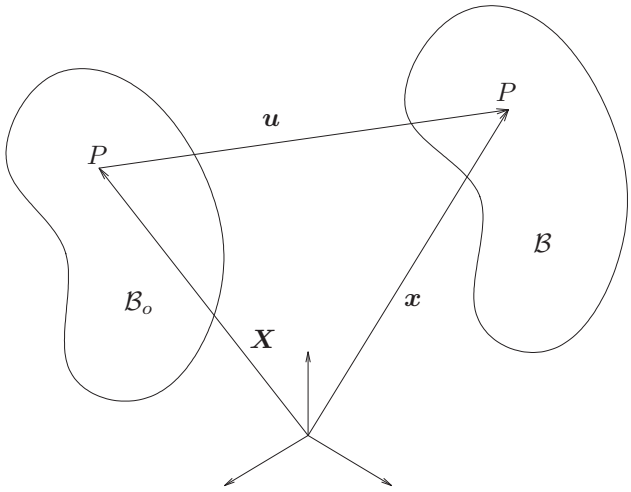

Figure 3.2: Undeformed and deformed configurations.

The coordinates of any point P within the body are given by $\boldsymbol{x}(P)$ in the deformed configuration and by $\boldsymbol{X}(P)$ in the undeformed configuration. The displacement of this point is denoted by $\boldsymbol{u}(P)$. It follows from Figure 3.2 that

$$\boldsymbol{x} = \boldsymbol{X} + \boldsymbol{u}. \tag{3.25}$$

The deformation gradient $\boldsymbol{F}$ is given by

$$\boldsymbol{F} = \frac{\boldsymbol{dx}}{\boldsymbol{dX}} = \boldsymbol{I} + \frac{d\boldsymbol{u}}{d\boldsymbol{X}}. \tag{3.26}$$

The Green-Lagrange strain tensor $\boldsymbol{E}$ is defined as

$$\boldsymbol{E} = \frac{1}{2}\left(\boldsymbol{F}^{\mathrm{T}}\boldsymbol{F} - \boldsymbol{I}\right). \tag{3.27}$$

We assume that the body is hyperelastic[39], from which it follows that the Cauchy stress tensor $\boldsymbol{T}$ is given by

$$\boldsymbol{T} = \frac{1}{\det(\boldsymbol{F})}\boldsymbol{F}\frac{De}{D\boldsymbol{E}}\boldsymbol{F}^{\mathrm{T}}. \tag{3.28}$$

where e is the strain energy function per unit volume in the initial configuration. $\frac{De}{D\boldsymbol{E}}$ is denoted the second Piola-Kirchoff stress tensor $\boldsymbol{S}$; it is symmetric.

Since the focus of this Chapter is to develop a geometrically nonlinear formulation, we only consider material models in which the second Piola Kirchoff stress is a linear function of the Green-Lagrange strain. In particular, we use a St-Venant-Kirchoff material, for which

$$e(\boldsymbol{E}) = \frac{\lambda}{2}\left(\text{tr}(\boldsymbol{E})\right)^2 + \mu \text{tr}(\boldsymbol{E}^2). \tag{3.29}$$

Here $\lambda > 0$ and $\mu > 0$ are the Lame constants. For this material $\boldsymbol{S} = \frac{De}{D\boldsymbol{E}} = \boldsymbol{\mathcal{C}}\boldsymbol{E}$, where $\boldsymbol{\mathcal{C}}$ contains the same constants that appear in the linear generalized Hooke's law, (3.2).

To summarize: In the domain Ω, the strong form of the geometrically nonlinear boundary value problem is given by:

$$\text{div}\boldsymbol{T} + \boldsymbol{f} = \boldsymbol{0}, \tag{3.30}$$
$$\boldsymbol{F} = \boldsymbol{I} + \nabla_X \boldsymbol{u}, \tag{3.31}$$
$$\boldsymbol{E} = \frac{1}{2}(\boldsymbol{F}^{\text{T}}\boldsymbol{F} - \boldsymbol{I}), \tag{3.32}$$
$$\boldsymbol{T} = \frac{1}{\det(\boldsymbol{F})}\boldsymbol{F}\boldsymbol{\mathcal{C}}\boldsymbol{E}\boldsymbol{F}^{\text{T}}, \tag{3.33}$$

and on the boundary Γ,

$$\boldsymbol{T}\cdot\boldsymbol{n} = \bar{\boldsymbol{t}} \quad \text{on} \quad \Gamma_t, \tag{3.34}$$
$$\boldsymbol{u} = \bar{\boldsymbol{u}} \quad \text{on} \quad \Gamma_u, \tag{3.35}$$

where ∇_X indicates spatial gradients w.r.t. the undeformed geometry and all other symbols have the same meaning as before.

The Tonti diagram in Figure 3.3 depicts the assumed stress mixed formulation of the geometrically nonlinear boundary value problem. The two primary fields, displayed in the filled boxes, are the displacement $\boldsymbol{u}$ and the second Piola-Kirchoff stress $\boldsymbol{S}$. The derived fields (or slave fields) that depend on the displacement field are $\boldsymbol{F}_u$ and $\boldsymbol{E}_u$. The field $\boldsymbol{E}_s$ is derived from the Piola-Kirchoff stress field. The Cauchy stress $\boldsymbol{T}$ depends on both the displacement field $\boldsymbol{u}$ (due to it's dependency on $\boldsymbol{F}_u$) and the Piola-Kirchoff stress $\boldsymbol{S}$, hence it is denoted $\boldsymbol{T}_{u,s}$.

Following a similar procedure as with the linear elastic assumed stress mixed formulation, the weak form of the geometrically nonlinear boundary value problem is stated as

$$\int_\Omega (\text{div}\boldsymbol{T} + \boldsymbol{f})\cdot\boldsymbol{w}_{\text{BE}} d\Omega = 0, \tag{3.36}$$
$$\int_{\Omega_o} (\boldsymbol{E}_u - \boldsymbol{E}_s)\cdot\boldsymbol{w}_{\text{CE}} d\Omega_o = 0, \tag{3.37}$$

where $\boldsymbol{w}_{\text{BE}}$ and $\boldsymbol{w}_{\text{CE}}$ have the same meaning as before. (3.36), the equilibrium condition, is enforced in the deformed (current) configuration, indicated by integration over the current domain Ω. The strain compatibility condition, (3.37), is enforced in the undeformed (original or reference) configuration, denoted by integration over the reference domain Ω_o. This follows since the Green-Lagrange strain is a strain measure defined in the undeformed (or reference) configuration.

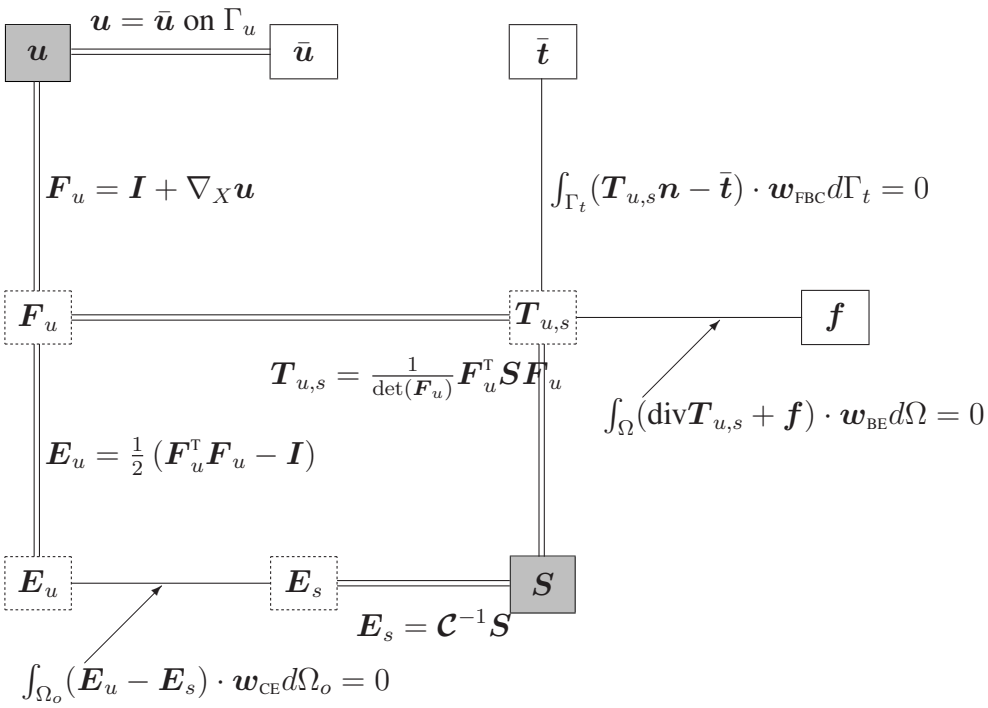

Figure 3.3: Tonti-diagram of geometrically nonlinear assumed stress mixed formulation.

Applying the divergence theorem to (3.36), and enforcing the traction boundary condition in a weak sense, we obtain

$$\int_{\Omega} (-\boldsymbol{T} \cdot \nabla_x \boldsymbol{w}_{\text{BE}} + \boldsymbol{f} \cdot \boldsymbol{w}_{\text{BE}}) d\Omega + \int_{\Gamma} \bar{\boldsymbol{t}} \cdot \boldsymbol{w}_{\text{BE}} d\Gamma = 0, \tag{3.38}$$

where ∇_x indicates spatial gradients w.r.t. the deformed (current) configuration.

3.3.1 Finite element formulation

The displacement field $\boldsymbol{u}$ and weighting function $\boldsymbol{w}_{\text{BE}}$ are interpolated as

$$\boldsymbol{u} = [N]\{U\} \quad \text{and} \quad \boldsymbol{w}_{\text{BE}} = [N]\{W_{\text{BE}}\}. \tag{3.39}$$

The gradient of the weighting functions follows as

$$\nabla_x \boldsymbol{w}_{\text{BE}} = [B_x]\{W_{\text{BE}}\}, \tag{3.40}$$

where the matrix $[B_x]$ contains the spatial gradients of the interpolation functions $[N]$ w.r.t. the deformed coordinates $\boldsymbol{x}$.

The Piola-Kirchoff stress vector $\{S\}$ is interpolated as

$$\{S\} = [P]\{\beta\}. \tag{3.41}$$

Note that since the Piola-Kirchoff stress field is defined in the reference configuration, the $[P]$ matrix only depends on the reference coordinates $\boldsymbol{X}$.

The Cauchy stress is computed from the second Piola-Kirchoff stress using (3.33). For convenient computer implementation in 2D plane problems, the Cauchy stress vector $\{T\}$ is computed as

$$\{T\} = \frac{1}{\det(\boldsymbol{F})}[\Upsilon]\{S\} = \frac{1}{\det(\boldsymbol{F})}[\Upsilon][P]\{\beta\}, \tag{3.42}$$

where

$$\{T\} = \begin{Bmatrix} T_{11} \\ T_{22} \\ T_{12} \end{Bmatrix}, \ \{S\} = \begin{Bmatrix} S_{11} \\ S_{22} \\ S_{12} \end{Bmatrix} \text{ and } [\Upsilon] = \begin{bmatrix} F_{11}^2 & F_{12}^2 & 2F_{11}F_{12} \\ F_{21}^2 & F_{22}^2 & 2F_{21}F_{22} \\ F_{11}F_{21} & F_{12}F_{22} & F_{11}F_{22} + F_{12}F_{21} \end{bmatrix}. \tag{3.43}$$

The vector form of the deformation gradient $\boldsymbol{F}$ is computed from

$$\{F\} = \begin{Bmatrix} F_{11} \\ F_{22} \\ F_{12} \\ F_{21} \end{Bmatrix} = [B_X]\{U\} + \begin{Bmatrix} 1 \\ 1 \\ 0 \\ 0 \end{Bmatrix}, \tag{3.44}$$

where $[B_X]$ contains the spatial gradients of the interpolation functions $[N]$ w.r.t. the reference coordinates $\boldsymbol{X}$.

Substituting (3.40) and (3.42) into (3.38), we obtain

$$\int_\Omega \{W_{\text{BE}}\}^{\text{T}} \left(-[B_x]^{\text{T}} \frac{1}{\det(\boldsymbol{F})}[\Upsilon][P]\{\beta\} + [N]^{\text{T}}\{f\} \right) d\Omega + \int_\Gamma \{W_{\text{BE}}\}^{\text{T}}[N]^{\text{T}}\{\bar{t}\} d\Gamma = 0. \tag{3.45}$$

Again, since $\{W_{\text{BE}}\}$ contains arbitrary nodal values, we obtain

$$\int_\Omega [B_x]^{\text{T}} \frac{1}{\det(\boldsymbol{F})}[\Upsilon][P]\{\beta\} d\Omega = \int_\Omega [N]^{\text{T}}\{f\} d\Omega + \int_\Gamma [N]^{\text{T}}\{\bar{t}\} d\Gamma. \tag{3.46}$$

For notational convenience, the right-hand side of (3.46) is henceforth denoted $\{\mathcal{F}\}$.

The stress interpolation parameters in $\{\beta\}$ are obtained via (3.37). The vector form of the Green-Lagrange strain $\{E_u\}$ is computed from

$$\{E_u\} = \begin{Bmatrix} E_{11} \\ E_{22} \\ 2E_{12} \end{Bmatrix} = \frac{1}{2} \begin{Bmatrix} F_{11}^2 + F_{12}^2 - 1 \\ F_{21}^2 + F_{22}^2 - 1 \\ 2(F_{11}F_{21} + F_{12}F_{22}) \end{Bmatrix}. \tag{3.47}$$

The Green-Lagrange strain vector $\{E_s\}$ is derived from the stress field, i.e.

$$\{E_s\} = [\mathcal{C}]^{-1}\{S\} = [\mathcal{C}]^{-1}[P]\{\beta\}. \tag{3.48}$$

Again, the weighting functions $\boldsymbol{w}_{\text{CE}}$ are interpolated using the interpolation matrix $[P]$, hence

$$\boldsymbol{w}_{\text{CE}} = [P]\{W_{\text{CE}}\}. \tag{3.49}$$

Substituting (3.47) through (3.49) into (3.37), we obtain

$$\int_{\Omega_o} \{W_{\text{CE}}\}^{\text{T}}[P]^{\text{T}} \left(\{E_u\} - [\mathcal{C}]^{-1}[P]\{\beta\}\right) d\Omega_o = 0. \tag{3.50}$$

Once again, since $\{W_{\text{CE}}\}$ contains arbitrary nodal quantities, we have

$$\int_{\Omega_o} [P]^{\text{T}}\{E_u\}d\Omega_o = \left(\int_{\Omega_o} [P]^{\text{T}}[\mathcal{C}]^{-1}[P]d\Omega_o\right)\{\beta\}. \tag{3.51}$$

The stress interpolation parameters in $\{\beta\}$ are solved from (3.51):

$$\{\beta\} = \left(\int_{\Omega_o} [P]^{\text{T}}[\mathcal{C}]^{-1}[P]d\Omega_o\right)^{-1} \int_{\Omega_o} [P]^{\text{T}}\{E_u\}d\Omega_o. \tag{3.52}$$

The formulation is completed by substituting (3.52) into (3.46) to obtain

$$\int_{\Omega} [B_x]^{\text{T}} \frac{1}{\det(\boldsymbol{F})}[\Upsilon][P]d\Omega \left(\int_{\Omega_o} [P]^{\text{T}}[\mathcal{C}]^{-1}[P]d\Omega_o\right)^{-1} \int_{\Omega_o} [P]^{\text{T}}\{E_u\}d\Omega_o = \{\mathcal{F}\}. \tag{3.53}$$

(3.53), which is a nonlinear equation in nodal displacements $\{U\}$, is now expressed as the residual equation

$$\{R\} = \int_{\Omega} [B_x]^{\text{T}} \frac{1}{\det(\boldsymbol{F})}[\Upsilon][P]d\Omega \left(\int_{\Omega_o} [P]^{\text{T}}[\mathcal{C}]^{-1}[P]d\Omega_o\right)^{-1} \int_{\Omega_o} [P]^{\text{T}}\{E_u\}d\Omega_o - \{\mathcal{F}\} = \{0\}. \tag{3.54}$$

We choose to solve (3.54) using the Newton-Raphson algorithm. If a trial solution $\{U\}_i$ is available at iteration i, the updated solution $\{U\}_{i+1}$ is solved from

$$\{U\}_{i+1} = \{U\}_i + \{\Delta U\}_{i+1}, \tag{3.55}$$

where the update $\{\Delta U\}_{i+1}$ is solved from the linear system of equations

$$\frac{d\{R\}_i}{d\{U\}_i}\{\Delta U\}_{i+1} = -\{R\}_i. \tag{3.56}$$

Should we attempt to solve (3.54) in the presented form, the computation of the consistent tangent $\frac{d\{R\}_i}{d\{U\}_i}$ is more difficult than necessary, because the integration of the first term occurs over the deformed configuration, which is a function of the unknown displacements. A simple transformation to the reference configuration is possible, using the relation

$$d\Omega = \det(\boldsymbol{F})d\Omega_o. \tag{3.57}$$

Substituting (3.57) into (3.54) produces the final form of the residual equation:

$$\{R\} = \sum_e \{R_e\} = \int_{\Omega_o} [B_x]^{\text{T}}[\Upsilon][P]d\Omega_o \left(\int_{\Omega_o} [P]^{\text{T}}[\mathcal{C}]^{-1}[P]d\Omega_o\right)^{-1} \int_{\Omega_o} [P]^{\text{T}}\{E_u\}d\Omega_o - \{\mathcal{F}_e\}, \tag{3.58}$$

where we have now explicitly indicated that the global residual $\{R\}$ is a summation over all the element residuals $\{R_e\}$.

If we consider the 2D plane problem, with n nodes per element, and p β parameters per element, we can conveniently express an element residual as

$$\{R_e\}_{2n\times 1} = [G]_{2n\times p}[H]^{-1}_{p\times p}\{M\}_{p\times 1} - \{\mathcal{F}_e\}_{2n\times 1}, \tag{3.59}$$

where the subscripts now indicate matrix and vector dimensions. The element matrices $[G]$ and $[H]$ and the element vector $\{M\}$ are respectively given by

$$[G]_{2n\times p} = \sum_{NGi}\sum_{NGj}[B_x]^{\mathrm{T}}[\Upsilon][P]\det(\boldsymbol{J})w_i w_j, \tag{3.60}$$

$$[H]_{p\times p} = \sum_{NGi}\sum_{NGj}[P]^{\mathrm{T}}[\mathcal{C}]^{-1}[P]\det(\boldsymbol{J})w_i w_j, \tag{3.61}$$

$$\{M\}_{p\times 1} = \sum_{NGi}\sum_{NGj}[P]^{\mathrm{T}}\{E_u\}\det(\boldsymbol{J})w_i w_j. \tag{3.62}$$

Note that we now explicitly indicate that the element matrices and vector are integrated numerically using Gauss quadrature, where NGi and NGj indicate the number of Gauss points, w_i and w_j are the Gauss point weights and $\boldsymbol{J}$ is the elemental Jacobian in the original configuration (hence not a function of the nodal displacements).

We compute the consistent tangent analytically, by assembly of the consistent tangents of each element. The consistent tangent of an element is computed by differentiating (3.59) w.r.t. the element nodal displacements $\{U_e\}$. The terms in (3.59) that depend on $\{U_e\}$ are $[G]$, $\{M\}$ and $\{\mathcal{F}_e\}$ (the last only if follower loads are present).

The element consistent tangent is computed as

$$\frac{d\{R_e\}}{d\{U_e\}} = \frac{d[G]}{d\{U_e\}}[H]^{-1}\{M\} + [G][H]^{-1}\frac{d\{M\}}{d\{U_e\}} - \frac{d\{\mathcal{F}_e\}}{d\{U_e\}}, \tag{3.63}$$

where

$$\frac{d[G]}{d\{U_e\}} = \sum_{NGi}\sum_{NGj}\left(\frac{d[B_x]^{\mathrm{T}}}{d\{U_e\}}[\Upsilon] + [B_x]^{\mathrm{T}}\frac{d[\Upsilon]}{d\{U_e\}}\right)[P]\det(\boldsymbol{J})w_i w_j, \tag{3.64}$$

$$\frac{d\{M\}}{d\{U_e\}} = \sum_{NGi}\sum_{NGj}[P]^{\mathrm{T}}\frac{d\{E_u\}}{d\{U_e\}}\det(\boldsymbol{J})w_i w_j. \tag{3.65}$$

The term $\frac{d[\Upsilon]}{d\{U_e\}}$ is constructed by differentiating (3.43) w.r.t. each component U_i of the nodal displacement vector $\{U_e\}$,

$$\frac{d[\Upsilon]}{dU_i} = \begin{bmatrix} 2F_{11}\frac{\mathrm{d}F_{11}}{dU_i} & 2F_{12}\frac{\mathrm{d}F_{12}}{dU_i} & 2\frac{\mathrm{d}F_{11}}{dU_i}F_{12} + 2\frac{\mathrm{d}F_{12}}{dU_i}F_{11} \\ 2F_{21}\frac{\mathrm{d}F_{21}}{dU_i} & 2F_{22}\frac{\mathrm{d}F_{22}}{dU_i} & 2\frac{\mathrm{d}F_{21}}{dU_i}F_{22} + \frac{\mathrm{d}F_{22}}{dU_i}F_{21} \\ \frac{\mathrm{d}F_{11}}{dU_i}F_{21} + \frac{\mathrm{d}F_{21}}{dU_i}F_{11} & \frac{\mathrm{d}F_{12}}{dU_i}F_{22} + \frac{\mathrm{d}F_{22}}{dU_i}F_{12} & \frac{\mathrm{d}F_{11}}{dU_i}F_{22} + \frac{\mathrm{d}F_{22}}{dU_i}F_{11} + \frac{\mathrm{d}F_{12}}{dU_i}F_{21} + \frac{\mathrm{d}F_{21}}{dU_i}F_{12} \end{bmatrix}. \tag{3.66}$$

The derivative $\frac{d\{F\}}{d\{U_e\}}$ is simply $[B_X]$, which follows directly from (3.44).

The derivative of the Green-Lagrange strain vector $\{E_u\}$ w.r.t. the nodal displacements is computed by differentiating (3.47):

$$\frac{d\{E_u\}}{d\{U_e\}} = \begin{Bmatrix} F_{11}\frac{dF_{11}}{d\{U_e\}} + F_{12}\frac{dF_{12}}{d\{U_e\}} \\ F_{21}\frac{dF_{21}}{d\{U_e\}} + F_{22}\frac{dF_{22}}{d\{U_e\}} \\ \frac{dF_{11}}{d\{U_e\}}F_{21} + F_{11}\frac{dF_{21}}{d\{U_e\}} + \frac{dF_{12}}{d\{U_e\}}F_{22} + F_{12}\frac{dF_{22}}{d\{U_e\}} \end{Bmatrix}. \tag{3.67}$$

The detailed computation of the matrices $[B_X]$, $[B_x]$ and the derivative $\frac{d[B_x]}{d\{U_e\}}$ are presented in the Appendix.

In the absence of follower loads, the consistent tangent is symmetric. In this case, the linear system in (3.56) is solved in the usual way by first factoring the consistent tangent using Cholesky decomposition, and then performing two backsubstitutions.

In linear elastic analysis, one criticism of mixed formulations is the computational cost of the matrix inversions required for the computation of every element stiffness matrix. For the nonlinear 5β element, the 5×5 matrix $[H]$ of course also requires inversion. Note however that this matrix is not a function of displacements, hence it remains constant during a geometrically nonlinear analysis. It is therefore possible to construct and invert the $[H]$ matrices for all the elements during the first iteration of nonlinear analysis, and then store them for all subsequent iterations. The total required storage space for all the $[H]$ matrices is approximately 40% of the storage requirement for the global consistent tangent, if the global consistent tangent is saved in sparse form.

3.3.2 Choice of interpolation matrix $[P]$

We use the same interpolation matrix $[P]$ as in the popular 5β linear elastic assumed stress mixed element [32] proposed by Pian and Sumihara. In this case, the matrix $[P]$ is given by

$$[P] = \begin{bmatrix} 1 & 0 & 0 & a_1^2\eta & a_3^2\xi \\ 0 & 1 & 0 & b_1^2\eta & b_3^2\xi \\ 0 & 0 & 1 & a_1b_1\eta & a_3b_3\xi \end{bmatrix}, \tag{3.68}$$

where ξ and η are the natural coordinates of the element. The parameters a_i and b_i are defined by

$$\begin{bmatrix} a_1 & b_1 \\ a_2 & b_2 \\ a_3 & b_3 \end{bmatrix} = \frac{1}{4}\begin{bmatrix} -1 & 1 & 1 & -1 \\ 1 & -1 & 1 & -1 \\ -1 & -1 & 1 & 1 \end{bmatrix}\begin{bmatrix} X_1 & Y_1 \\ \vdots & \vdots \\ X_4 & Y_4 \end{bmatrix}, \tag{3.69}$$

where X_i and Y_i are the reference coordinates of node i.

The parameters a_i and b_i constrain the stress interpolation matrix; a number of alternative constraints to those proposed by Pian and Sumihara are possible. A selection was proposed by Di and Ramm [41]. However, our experience with linear elements suggests that the difference in accuracy due to alternative constraint formulations is not expected to be dramatic. Therefore we only consider $[P]$ as in (3.68) and (3.69).

3.4 Numerical results

3.4.1 Patch tests

As expected, the element passes the uniaxial and simple shear patch tests. The undeformed and deformed patch of elements for the prescribed displacement simple shear test are depicted in Figure 3.4 (a) and (b) respectively. This specific example is a plane stress analysis with $E = 1.0$, $\nu = 0.3$ and unit thickness. The norm of the residual vector $\{R\}_i$ and the norm of the displacement increment $\{\Delta U\}_i$ are listed in Table 3.1 versus iterations number i. Since all stress and strain components are non-zero for this problem, the observed quadratic convergence rate per iteration (not to be confused with quadratic convergence rate with mesh refinement) verifies that the consistent tangent is computed correctly.

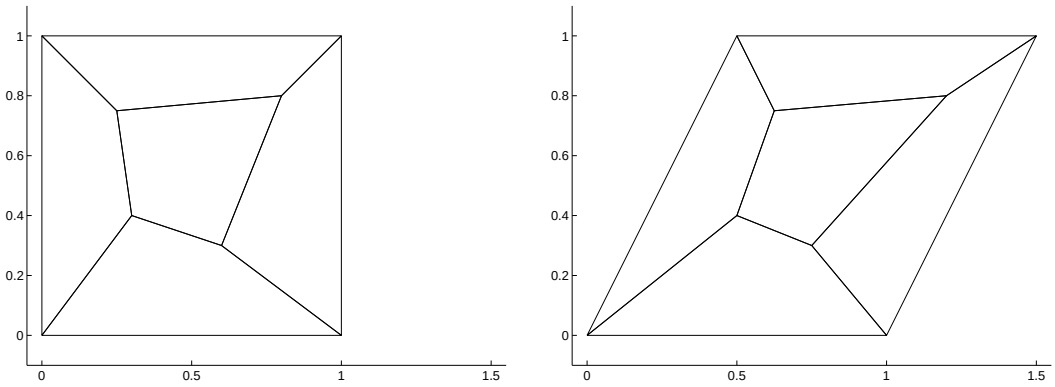

Figure 3.4: (a) Undeformed and (b) deformed simple shear patch.

Iteration #	$\|\{R\}_i\|$	$\|\{\Delta U\}_i\|$
1	5.946419	3.916557×10^{-1}
2	1.736318	1.891666×10^{-1}
3	4.459804×10^{-1}	1.189603×10^{-1}
4	9.868668×10^{-2}	3.721763×10^{-2}
5	1.113266×10^{-2}	5.123944×10^{-3}
6	1.916301×10^{-4}	$8.48968e \times 10^{-5}$
7	5.557537×10^{-8}	$2.42351e \times 10^{-8}$
8	4.565369×10^{-15}	1.987818×10^{-15}

Table 3.1: Convergence history for simple shear patch test depicted in Figure 3.4.

3.4.2 Pure flexure of a beam

In order to assess the performance of the mixed element in bending dominated problems, we analyze a beam of length 10 and depth 1, that is bent into a complete circle. The problem is

analyzed with $E = 1.0$ and $\nu = 0$. As the solution to this problem contains no singularities, this example will be used to numerically compute the convergence rate of our proposed nonlinear element, as the mesh is refined. We expect a convergence rate of 2, similar to the linear elastic version of our element.

In the finite element simulation, the beam is only constrained at the left and right edges, which are forced to coincide. The initial guess of the deformed shape is given by

$$x = (R - Y)\sin(X/R), \tag{3.70}$$
$$y = R - (R - Y)\cos(X/R), \tag{3.71}$$

where X and Y are the undeformed coordinates, x and y are the deformed coordinates and $R = L/2\pi$ is the radius of the neutral axis. The moment required to deform the beam into the circle is computed from the nodal reactions after the analysis converges. A finite-difference based numerical solution to this problem [42], using 10000 point through the thickness of the beam, predicts that a moment of 0.0432523 will bend the beam into a complete circle.

The computed moments are listed in Table 3.2 for a number of meshes, where they are also compared to the linear 4 node element (Q4) and the quadratic 8 node element using both full integration (Q8FI) and reduced integration (Q8RI). These results are also depicted graphically in Figure 3.5, which illustrates that the convergence rate of the proposed mixed element is indeed 2. Note that the convergence rate of the Q8 elements is 4, higher that the expected rate of 3. An example of a deformed mesh is given in Figure 3.6, which depicts the 40×4 mesh.

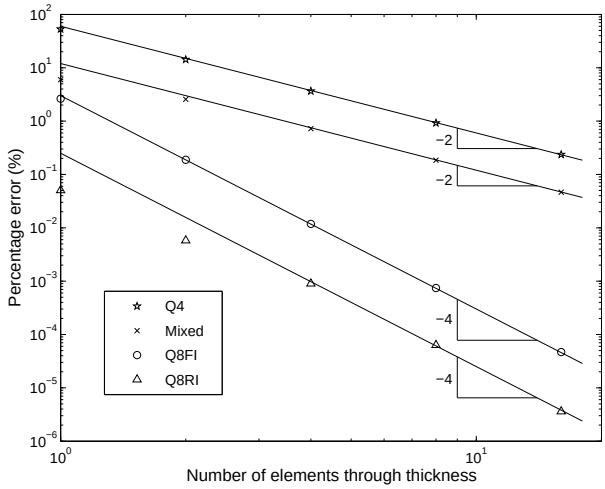

Figure 3.5: Convergence of the required moment to bend the beam into a complete circle.

3.4.3 Cook's membrane

Consider the tapered panel depicted in Figure 3.7, which is clamped at the left edge and subjected to a shear load on the right edge. This problem is known as 'Cook's membrane problem' in the linear elastic case [38]. The plane stress simulation is performed with $E = 1.0$, $\nu = 0.3$ and unit thickness. The nodal loads are computed for a uniform transverse load distribution in the reference configuration, and does not change with displacement.

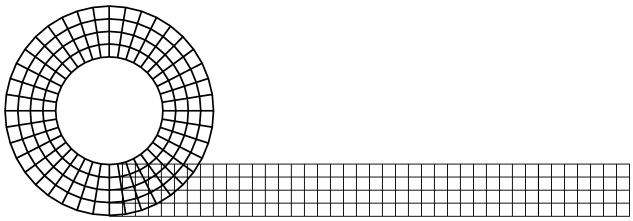

Figure 3.6: Deformed shape of a deep beam subject to a pure bending moment.

Mesh size	Tip moment			
	mixed	Q4	Q8FI	Q8RI
10×1	0.0458336	0.0661433	0.0443912	0.0432741
20×2	0.0443630	0.0494159	0.0433339	0.0432498
40×4	0.0435642	0.0448334	0.0432574	0.0432519
80×8	0.0433323	0.0436502	0.0432526	0.0432522
160×16	0.0432724	0.0433544	0.0432523	0.0432523

Table 3.2: Tip moments required to bend a deep beam into a complete circle.

In the linear elastic case this problem is usually solved for a total transverse load magnitude of 1.0 upwards. However, in the geometrically nonlinear version of this problem, this load magnitude is excessive in the limit of mesh refinement, as the top left element inverts. Hence, we perform a mesh refinement study with the unit load applied downwards, which does not lead to element inversion anywhere in the mesh.

Note that this problem contains a singularity in the strain and stress fields at the left top corner, point A in Figure 3.7. Therefore, the theoretical convergence rate of elements no longer applies, and the strength of the singularity generally dictates the convergence rate [38]. Since many practical problems contain singularities, this example is used to demonstrate the accuracy of the proposed element in such a case.

# elements in mesh	Nonlinear Q4	Nonlinear Q8RI	Nonlinear mixed
2×2	-12.9801	-27.4169	-24.9396
4×4	-21.5895	-28.2439	-27.7063
8×8	-26.3671	-28.3897	-28.2568
16×16	-27.8926	-28.4387	-28.3993
32×32	-28.3095	-28.4580	-28.4437
64×64	-28.4233	-28.4653	-28.4598
128×128	-28.4557	-28.4681	-28.4659

Table 3.3: Vertical displacement at the center of the right edge for Cook's membrane problem as a function of the number of elements in the mesh.

The downwards vertical displacement at the center of the right edge, point C in Figure 3.7, is tabulated in Table 3.3 as a function of the number of elements per mesh. An example of the

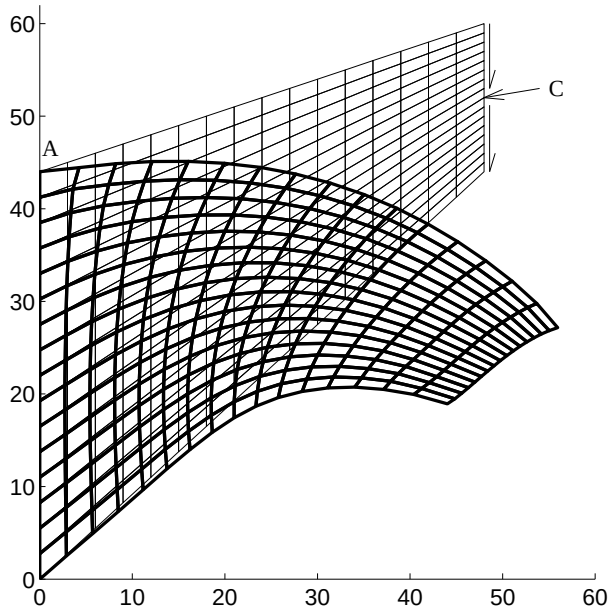

Figure 3.7: Undeformed and deformed Cook's membrane problem for the 16×16 mesh.

deformed shape is presented in Figure 3.7, which depicts the 16×16 mesh. The accuracy of the mixed element is compared to the geometrically nonlinear displacement-based elements Q4 and Q8RI in Table 3.3. The displacement results are also presented graphically in Figure 3.8 as a function of the total number of degrees of freedom. This illustrates that for problems with singularities, our 4 node mixed formulation demonstrates similar accuracy as the Q8RI element, when expressed as a function of the total number of structural degrees of freedom.

The analysis was repeated for the 32×32 mesh for a tip load varying between -1 and 1. The vertical displacement of point C as a function of the total load magnitude is summarized in Table 3.4. The resulting load-displacement graph is depicted in Figure 3.9. Note the hardening behavior for a positive force (the moment arm decreases as the beam deflects upwards) and the softening behavior for a negative force (the moment arm increases as the beam deflects downwards).

Load	Displacement	Load	Displacement
1.0	15.3352	-1.0	-28.4437
0.8	13.2546	-0.8	-23.0137
0.6	10.8323	-0.6	-17.1295
0.4	7.9203	-0.4	-11.0468
0.2	4.3592	-0.2	-5.1987
0.1	2.2861	-0.1	-2.4998
0.01	0.23832	-0.01	-0.24047
0.001	0.023929	-0.001	-0.023951

Table 3.4: Cook's membrane: Tip midpoint deflection vs. total transverse load.

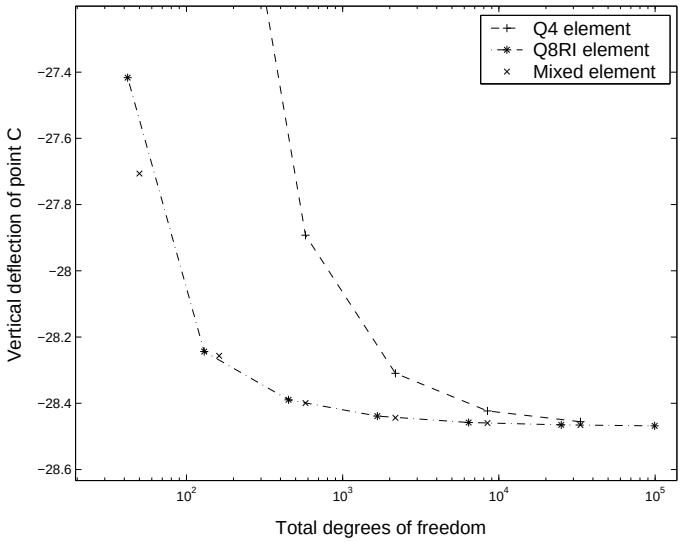

Figure 3.8: Cook's membrane problem: Convergence of the vertical tip displacement.

3.4.4 Beam under tip load

In this example [37], a cantilever beam of unit height and length $L = 20$, subjected to a transverse load P, is studied. The problem is analyzed using our mixed formulation, as well as the displacement based Q4 and Q8RI elements, for $E = 4.8 \times 10^8$ and $\nu = 0$ (in which case plane stress and plane strain are identical).

The beam theory analytical solution, which does not take through thickness effects into account, is available from [43]. Results are presented in terms of the normalized force $\frac{PL^2}{EI}$ and the normalized vertical tip deflection $\frac{W}{L}$, where W is the vertical tip deflection and I is the second moment of area of the beam cross section.

Figure 3.10 compares the accuracy of the mixed element to the analytical solution, as well as the Q4 and Q8RI elements. Note that the mixed element solution using a 10×1 mesh compares almost exactly to the analytical solution. Although not shown here, the agreement deteriorates slightly with mesh refinement, as through thickness effects start playing a role (not accounted for in the analytical solution). The Q8RI result also demonstrates this effect, with predicted tip displacement slightly greater than the analytical value. Examples of deformed states are depicted in Figure 3.11, for various values of the normalized force P_N.

3.5 Conclusions

In this Chapter, a geometrically nonlinear version of the popular 5β assumed stress element previously proposed by Pian and Sumihara for linear elasticity was developed. The resultant element is rank sufficient and passes the patch test. In the presence of singularities, the accuracy of the element is comparable to that of the well known displacement based Q8 element with a quadratic interpolation field and reduced integration.

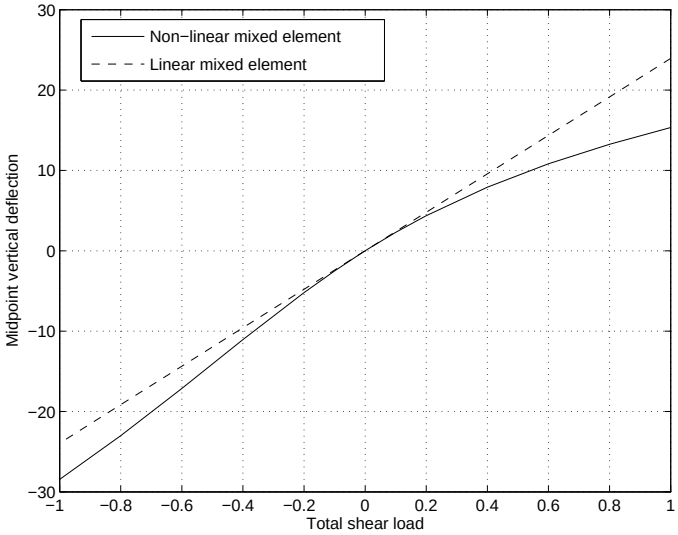

Figure 3.9: Load-displacement graph for Cook's membrane problem, which illustrates softening and hardening response.

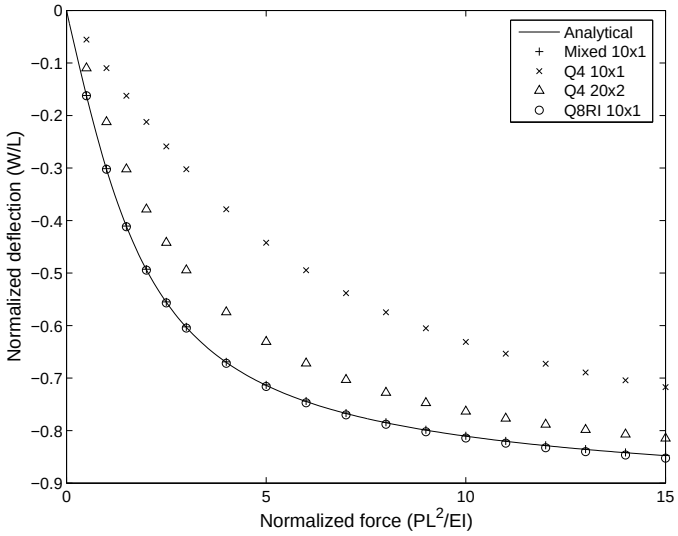

Figure 3.10: Force-displacement comparison for transverse loading of a cantilever beam.

Like the element for linear elasticity, the element requires inversions of the partition matrix $[H]$ on the element level. However, since this matrix is not a function of elemental displacements, it remains constant during a geometrically nonlinear analysis. This fact may be exploited in an efficient computer implementation, if so desired.

Numerical results confirm the accuracy of the element. The element is an attractive alternative to the displacement based Q4 element in implicit finite element codes; in particular in (slender) bending dominated applications.

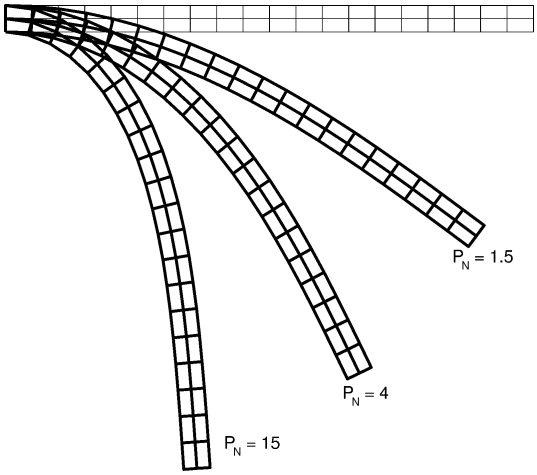

Figure 3.11: Deformation of cantilever beam with increasing transverse tip load, obtained using a 20×2 mesh and the mixed element.

Chapter 4

FE modeling of MEMS, using analytical gradients

In this chapter, an efficient algorithm for self-consistent analysis of electromechanical coupled systems in MEMS is described. The algorithm employs a Newton method to solve the coupled electromechanical equations using *analytical gradients*. This approach is shown to converge very rapidly and is much faster than the simpler relaxation algorithm for tightly coupled cases. While this chapter focuses on coupled electromechanical analysis, the proposed algorithm can be extended to include several coupled domains typically encountered in MEMS.

4.1 Introduction

The progress of MEMS is growing rapidly in recent years and the potential of MEMS is widely recognized. MEMS devices are increasingly used in various fields such as the aerospace and automotive industries. MEMS mechanisms typically exploit the interaction of multiple physical fields, and modeling and simulation of the coupled fields plays a very important role in the design phase in predicting device characteristics. In traditional deterministic MEMS design, this coupling is often roughly approximated, leading to performance and reliability problems [44]. In recent years, finite-element (FE) based simulation tools are frequently used in designing MEMS devices.

Although there are many MEMS designs that use piezoelectric, thermal, pneumatic, and magnetic actuation, a very popular approach in present day microsensor and microactuator designs is to use electrostatic forces to move micromachined parts [45]. Electrostatic MEMS is a special branch under micromechanics with a wide range of applications such as switches, micro-mirrors and micro-resonators [46]. Analysis of such microelectromechanical systems involves two coupled fields: electrostatics and elastomechanics.

The elastomechanics can sometimes be geometrically nonlinear due to either large deflection or nonlinear stiffening. For the geometrically linear case, the structure is analyzed in the undeformed (original) configuration; while for the geometrically nonlinear case, the structural stiffness is no longer constant, hence the structure is solved in the deformed (current) shape. If a case is analyzed where large deflections occur, such as a slender beam subjected to a large electrostatic force, un-

structured remeshing may be required to generate the electrical mesh, in order to avoid element inversions. In cases where the geometric nonlinearity does not coincide with large deflections, such as stress-stiffening in clamped membranes, a simpler structured remeshing algorithm can be used to generate the electrical mesh.

Newton's method is an attractive option to solve the coupled non-linear system. But the gradients required in the Newton method are normally approximated using finite-differences. When the systems become complex, many degrees of freedom are required to model it accurately, therefore the cost of evaluation of the gradients using finite-differences could be enormous.

MEMS are often designed on scales at which electrostatic forces are capable of moving or deforming the parts of the system. In this regime accurate prediction of device behavior may require 3-D coupled simulations between the electrostatic and mechanical domains [5]. However, in many cases a 2-D model can be very accurate. In fact, as shown in Reference [47], a 2-D model for a electrostatic-mechanical coupled cantilever beam gives an error of less than 1%.

In this chapter, FEM is used to model 2-D coupled fields and the gradients for the 2-D model used during a Newton iteration are expressed analytically without using finite-differences. The analytic gradients provide the accuracy and efficiency required for the analysis. With examples, it will be shown that Newton's method can solve the coupled field system very efficiently using analytical gradients, even when the unstable pull-in stage is approached. A few other common methods are also studied for comparison.

The chapter is concluded by analyzing two problems in which geometric nonlinearities occur. The first problem concerns the large deflection of a slender cantilever beam subjected to a electrostatic force. The maximum deflection of the beam tip is limited by inversion of electrical elements, due to the use of a structured remeshing algorithm. The second problem analyses the effect of stress-stiffening in a clamped membrane. In this case, the structured remeshing of the electrical mesh performs well.

4.2 Electrostatics and elastomechanics systems

Microelectromechanical systems involve a mechanical structure which deforms when subjected to electrostatic actuation, as shown in Figure 4.1. Typically, the deformation will cause a change in the charge distribution, and 'reorganization' of the structure (and the electrical field around it), as illustrated in Figure 4.1. An equilibrium state is reached when the mechanical force due to the deformation of the structure and the electrostatic force due to the electrical charges balance each other. The final deformation and charge distribution can be obtained by solving the non-linear coupled system iteratively.

In linear structural analysis the assumption is made that the displacement gradients are *very* small, hence the structural stiffness remains constant throughout the analysis. In a FEM analysis this means that geometry of the elements remains basically unchanged in the loading process and that strains can be approximated by the first-order, infinitesimal linear form [48]. These assumption are no longer valid in many problems involving microsensors and particularly microactuators, in which large displacement gradients may occur [49]. Geometrical non-linearities must be introduced, besides the non-linearities due to the electromechanical coupling.

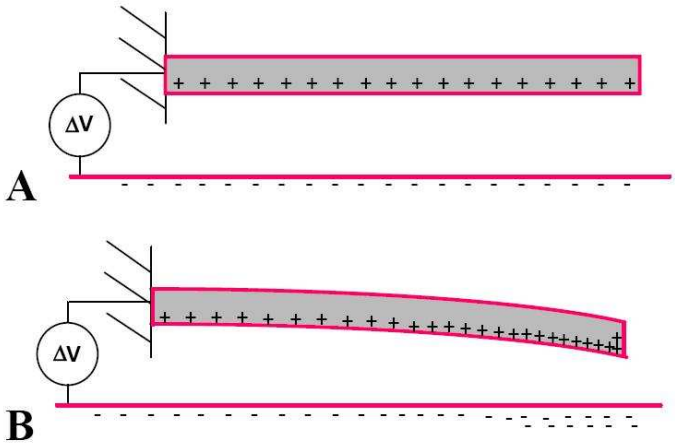

Figure 4.1: A schematic figure showing the reorganization of charge (and thus forces) accompanying the deformation in an electro-mechanical device.

4.2.1 Structural modeling

In this chapter, we consider geometrically nonlinear structural analysis. The possible simplifications in the case of linear structural analysis will be noted. Mathematically, the discretized residual equation of the elastostatic field is represented as

$$\boldsymbol{R}_s(\boldsymbol{u}, \boldsymbol{V}) = \boldsymbol{f}_{\text{int}}(\boldsymbol{u}) - \boldsymbol{f}_{\text{ext}}(\boldsymbol{u}, \boldsymbol{V}) \tag{4.1}$$

where $\boldsymbol{f}_{\text{int}}$ and $\boldsymbol{f}_{\text{ext}}$ are the internal and external nodal loads respectively. In the case of a linear elastic structural analysis, $\boldsymbol{f}_{\text{int}} = \boldsymbol{K}_s\boldsymbol{u}$, where $\boldsymbol{K_s}$ is the stiffness matrix of the structure and $\boldsymbol{u}$ is the nodal displacements. In this chapter, we only consider electrostatic forces. Therefore, the external nodal load $\boldsymbol{f}_{\text{ext}}$ depend on the voltage field $\boldsymbol{V}$ of the electrostatic field. However, due to the choice of a structured remeshing strategy to generate the electrical mesh, the nodal coordinates of all the electrical elements depend on the structural displacements $\boldsymbol{u}$. The external nodal force vector $\boldsymbol{f}_{\text{ext}}$ therefore depends on both the voltage $\boldsymbol{V}$ and the displacement $\boldsymbol{u}$.

4.2.2 Electrostatic modeling

The electrostatic field can also be discretized and the residual equation for the electrostatic field is written as

$$\boldsymbol{R}_e(\boldsymbol{u}, \boldsymbol{V}) = \boldsymbol{K}_e(\boldsymbol{u})\boldsymbol{V} - \boldsymbol{q} \tag{4.2}$$

where $\boldsymbol{K}_e$ represents the permittivity matrix of the electrostatic field and $\boldsymbol{q}$ is the nodal charge density of the electrostatic field. Note that in the discretized governing equation, the nodal voltage $\boldsymbol{V}$ is a vector.

4.2.3 Remeshing

For a computed structural displacement $\boldsymbol{u}$, there are two mesh generation options for the electrostatic mesh. Firstly, an adaptive scheme can be used in conjunction with a structured electrostatic mesh; secondly, given a structural displacement $\boldsymbol{u}$, a completely new electrostatic mesh can be generated at every iteration. In this chapter, the first mentioned structured remeshing strategy is used. In order to do so, a third field is introduced to describe the motion of the structured electrostatic mesh. The deformation of the electrostatic domain is modeled by a finite element formulation of a fictitious elastic structure.

The purpose of introducing these fake structural elements is to limit elemental distortions and adjust node locations within the electrostatic domain. The structural displacements are imposed on the electrostatic mesh along the common interface.

In the work by Allen *et. al.* [44], such a three-field formulation is used to allow for relatively large deformations of the electrostatic domain due to elastic displacements of the structure and structural shape changes in an optimization process. In our case, we opt for the same three-field formulation in order to generate analytical gradients, in particular the gradients of the electrical mesh coordinates w.r.t. the structural displacement $\boldsymbol{u}$.

The deformed electrostatic mesh is generated by solving the following fictitious mechanical residual equation

$$\boldsymbol{R}_f(\boldsymbol{u}) = \boldsymbol{K}_f \boldsymbol{w}(\boldsymbol{u}) - \boldsymbol{g} \tag{4.3}$$

where $\boldsymbol{K}_f$ is the fictitious stiffness matrix of the electrostatic mesh, $\boldsymbol{w}$ is the electrostatic mesh displacement and $\boldsymbol{g}$ is the fictitious nodal loads.

4.2.4 Newton-Raphson method

Note that since (4.3) is a simple linear equation, the electrostatic mesh displacement $\boldsymbol{w}$ is treated as a dependent variable i.e. $\boldsymbol{w} = \boldsymbol{w}(\boldsymbol{u})$. Therefore, there are only two residuals ($\boldsymbol{R}_s$ and $\boldsymbol{R}_e$) in the coupled system, which depend on the two independent variables $\boldsymbol{u}$ and $\boldsymbol{V}$.

We therefore solve the nonlinear system

$$\left\{ \begin{array}{c} \boldsymbol{R}_s(\boldsymbol{u},\boldsymbol{V}) \\ \boldsymbol{R}_e(\boldsymbol{u},\boldsymbol{V}) \end{array} \right\} = \left\{ \begin{array}{c} \boldsymbol{f}_{\text{int}}(\boldsymbol{u}) - \boldsymbol{f}_{\text{ext}}(\boldsymbol{u},\boldsymbol{V}) \\ \boldsymbol{K}_e(\boldsymbol{u})\boldsymbol{V} - \boldsymbol{q} \end{array} \right\} = \left\{ \begin{array}{c} \boldsymbol{0} \\ \boldsymbol{0} \end{array} \right\} \tag{4.4}$$

iteratively for $\boldsymbol{u}$ and $\boldsymbol{V}$ from the Newton-Raphson method, i.e.

$$\left[\begin{array}{cc} \frac{\partial \boldsymbol{R}_s}{\partial \boldsymbol{u}} & \frac{\partial \boldsymbol{R}_s}{\partial \boldsymbol{V}} \\ \frac{\partial \boldsymbol{R}_e}{\partial \boldsymbol{u}} & \frac{\partial \boldsymbol{R}_e}{\partial \boldsymbol{V}} \end{array} \right]^i \left\{ \begin{array}{c} \Delta \boldsymbol{u} \\ \Delta \boldsymbol{V} \end{array} \right\}^i = - \left\{ \begin{array}{c} \boldsymbol{R}_s \\ \boldsymbol{R}_e \end{array} \right\}^i \tag{4.5}$$

where $\Delta \boldsymbol{u}^i$ and $\Delta \boldsymbol{V}^i$ is the solution update at iteration i. The updated values for $\boldsymbol{u}$ and $\boldsymbol{V}$ is then computed from

$$\left\{ \begin{array}{c} \boldsymbol{u} \\ \boldsymbol{V} \end{array} \right\}^{i+1} = \left\{ \begin{array}{c} \boldsymbol{u} \\ \boldsymbol{V} \end{array} \right\}^i + \left\{ \begin{array}{c} \Delta \boldsymbol{u} \\ \Delta \boldsymbol{V} \end{array} \right\}^i . \tag{4.6}$$

(4.5) and (4.6) are solved repeatedly until the norm of both residuals are sufficiently close to zero, and/or the solution converges. Note that the above expressions already presume that the prescribed displacements and voltages have been applied, and that the reduced system is being solved.

4.3 The residuals and analytical gradients

In this section, the residuals ($\boldsymbol{R}_s$ and $\boldsymbol{R}_e$) and analytical gradients in (4.5) are derived for a 2-D analysis. (The 3-D analytical gradients can of course be obtained in a similar manner.)

4.3.1 The structural residual

The structural residual $\boldsymbol{R}_s$ is computed from (4.1). The computation of the internal nodal load $\boldsymbol{f}_{\text{int}}$, using a nonlinear mixed formulation, is detailed in Chapter 3. For example, $\boldsymbol{f}_{\text{int}}$ is the first term in (3.59). To complete the computation of the structural residual, we require the external nodal load vector $\boldsymbol{f}_{\text{ext}}$, due to the electrostatic field.

Electrostatic load

The electrostatic pressure is given by Maxwell's electrostatic stress tensor evaluated along the structural interface $\Omega_{e/s}$ in the electrostatic mesh [50]. Assuming the structure to be a perfect conductor, the electrostatic stress tensor is

$$\boldsymbol{T}_e = \epsilon_0 \boldsymbol{e} \otimes \boldsymbol{e} - \frac{1}{2}\epsilon_0 \|\boldsymbol{e}\|^2 \boldsymbol{I} \tag{4.7}$$

where $\boldsymbol{e} = \nabla V = [e_x, e_y]^T$ is the electrostatic field, ϵ_0 is the permittivity of the free space, $\boldsymbol{I}$ is the second order identity tensor and $\otimes$ is the dyadic product. Using the usual finite element notation, the electrostatic field is written as

$$\boldsymbol{e} = \nabla V = \left\{ \begin{array}{c} e_x \\ e_y \end{array} \right\} = [B_x]\{V\} \tag{4.8}$$

where $[B_x]$ contains the spatial gradients of the voltage interpolation functions. Note that these gradients are taken w.r.t. the current coordinates of the electrical mesh (which depend on the structural displacement).

The matrix form of the electrostatic stress tensor for two dimensions is written as

$$[T_e] = \epsilon_0 \left[\begin{array}{cc} e_x^2 - \frac{1}{2}\|\boldsymbol{e}\|^2 & e_x e_y \\ e_x e_y & e_y^2 - \frac{1}{2}\|\boldsymbol{e}\|^2 \end{array} \right]. \tag{4.9}$$

The electrostatic pressure is given as

$$\boldsymbol{P} = \boldsymbol{T_e} \boldsymbol{n} \tag{4.10}$$

where $\boldsymbol{n}$ is the normal on $\Omega_{e/s}$, pointing from the structural mesh into the electrical mesh. The electrostatic force, here acting as an external force on the structure, is computed as

$$\boldsymbol{f}_{\text{ext}} = \int_{\Omega_{e/s}} \boldsymbol{P} d\Omega_{e/s}. \tag{4.11}$$

As (4.10) shows, the electrostatic force is computed along the structural-electrostatic interface; it is clear that the electrostatic force depends on the coordinates of the nodes in both the structural

and electrostatic meshes. Figure 4.2 illustrates this point: the coordinates of nodes 1 and 4 depend on the electrostatic mesh; while the coordinates of nodes 2 and 3 depend on the structural mesh. In this case, the electrical nodal pressure for edge 2-3 contains four components

$$\{P_n\} = \begin{bmatrix} P_{2_x} & P_{2_y} & P_{3_x} & P_{3_y} \end{bmatrix}^T. \tag{4.12}$$

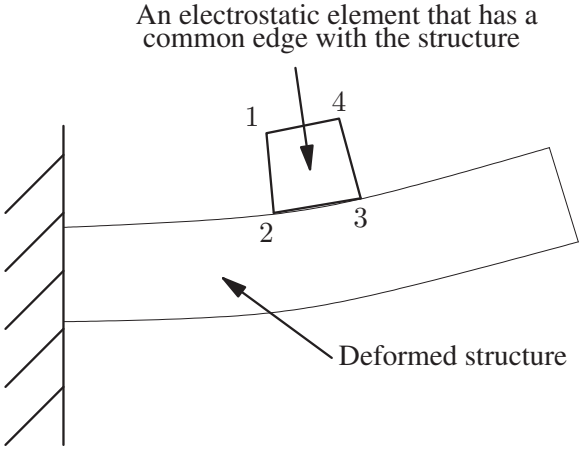

Figure 4.2: The interface electrostatic element.

Once the electrical pressure at the two nodes are known, it is then interpolated along the interface $\Omega_{e/s}$

$$\boldsymbol{P} = [N]\{P_n\} \tag{4.13}$$

where $[N]$ is the interpolation matrix. The electrical nodal force then becomes

$$\boldsymbol{f}_{\text{ext}} = \int_{\Omega_{e/s}} [N] d\Omega_{e/s} \{P_n\} \tag{4.14}$$

The integration result $[M]$ of a linear interpolation matrix can be found in Appendix B. The electrical nodal force is therefore

$$\{f_{\text{ext}}\} = [M]\{P_n\} = \begin{bmatrix} f_{2_x} & f_{2_y} & f_{3_x} & f_{3_y} \end{bmatrix}^T. \tag{4.15}$$

As shown in Figure 4.3, the electrostatic nodal pressure $\{P_n\}$ is interpolated and then integrated to obtain the electrostatic nodal loads $\{f_{\text{ext}}\}$.

The computation of the structural residual is now complete, and the gradient computation now follows.

4.3.2 Gradients of the structural residual

Gradient of the structural residual with respect to displacement

Direct differentiation of (4.1) w.r.t. displacement gives

$$\frac{\partial \boldsymbol{R}_s}{\partial \boldsymbol{u}} = \frac{\partial \boldsymbol{f}_{\text{int}}}{\partial \boldsymbol{u}} - \frac{\partial \boldsymbol{f}_{\text{ext}}}{\partial \boldsymbol{u}}. \tag{4.16}$$

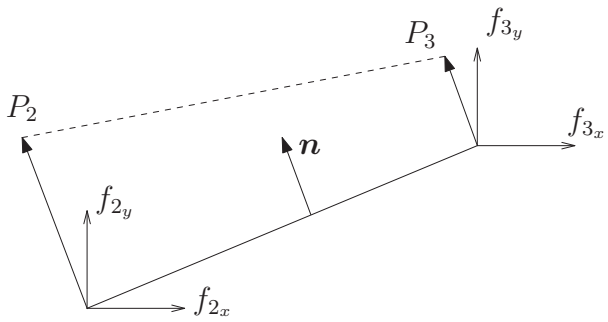

Figure 4.3: Interpolation of the electrical pressure.

The derivative of the external load vector w.r.t. displacement, for the case of a geometrically non-linear mixed formulation, is detailed in Chapter 3. In the case of a structurally linear analysis, this derivative simply reduces to the structural stiffness matrix $\boldsymbol{K}_s$.

The derivative of the internal load vector w.r.t. displacement follows from appolication of the chain rule, i.e.

$$\frac{\partial \boldsymbol{f}_{\text{ext}}}{\partial \boldsymbol{u}} = \frac{\partial \boldsymbol{f}_{\text{ext}}}{\partial \boldsymbol{x}} \frac{\partial \boldsymbol{x}}{\partial \boldsymbol{u}} \tag{4.17}$$

where $\boldsymbol{x}$ is the current coordinates of all the nodes within the mesh of the system. This includes both the structural mesh and the electrostatic mesh, i.e.

$$\boldsymbol{x} = [\boldsymbol{x}_s, \boldsymbol{x}_e]^T \tag{4.18}$$

where $\boldsymbol{x}_s$ represents the current coordinates of the nodes in the structural mesh and $\boldsymbol{x}_e$ represents the current coordinates of the nodes in the electrostatic mesh. This gradient is computed for each element, and assembled in the usual manner to provide the total gradient.

The two required terms $\frac{\partial \boldsymbol{f}_{\text{ext}}}{\partial \boldsymbol{x}}$ and $\frac{\partial \boldsymbol{x}}{\partial \boldsymbol{u}}$ are now discussed in detail, at element level.

First, the term $\frac{\partial \{f_{\text{ext}}\}}{\partial \{x\}}$ is considered. From (4.10) and (4.15), we get

$$\frac{\partial \{f_{\text{ext}}\}}{\partial \{x\}} = [M] \frac{\partial [T_e]}{\partial \{x\}} \{n\} + [M]\,[T_e] \frac{\partial \{n\}}{\partial \{x\}}. \tag{4.19}$$

$\frac{\partial [T_e]}{\partial \{x\}}$ follows from the chain rule of differentiation, to get

$$\frac{\partial [T_e]}{\partial \{x\}} = \frac{\partial [T_e]}{\partial \{e\}} \frac{\partial \{e\}}{\partial \{x\}} = \frac{\partial [T_{e_x}]}{\partial e_x} \frac{\partial e_x}{\partial \{x\}} + \frac{\partial [T_e]}{\partial e_y} \frac{\partial e_y}{\partial \{x\}}. \tag{4.20}$$

$\frac{\partial [T_e]}{\partial \{e\}}$ follows from direct differentiation of (4.9):

$$\frac{\partial [T_e]}{\partial e_x} = \epsilon_0 \begin{bmatrix} e_x & e_y \\ e_y & -e_x \end{bmatrix} \quad \text{and} \quad \frac{\partial [T_e]}{\partial e_y} = \epsilon_0 \begin{bmatrix} -e_y & e_x \\ e_x & e_y \end{bmatrix}. \tag{4.21}$$

From the definition of the electrostatic field in (4.8), it is found that

$$\frac{\partial \{e\}}{\partial \{x\}} = \frac{\partial [B_x]}{\partial \{x\}} \{V\}. \tag{4.22}$$

The derivative of the kinematic matrix $[B_x]$ with respect to the current coordinates $\{x\}$ is given in Appendix B.

The normal on an edge of a 2-D element is defined as:

$$\{n\} = \frac{1}{L_e} \begin{Bmatrix} \Delta y \\ -\Delta x \end{Bmatrix} \tag{4.23}$$

where Δy and Δx are the differences of the coordinates of the nodes connecting the edge of the element, and $L_e = \sqrt{\Delta x^2 + \Delta y^2}$ is the length of the element edge. Therefore, $\frac{\partial\{n\}}{\partial\{x\}}$ can be computed, using the chain rule.

All the terms required in (4.19) have now been discussed. We now turn our attention to the computation of $\frac{\partial \boldsymbol{x}}{\partial \boldsymbol{u}}$, which will complete the gradient computation in (4.17).

From (4.18), we have

$$\frac{\partial\{x\}}{\partial\{u\}} = \frac{\partial\left[\{x_s\},\{x_e\}\right]^T}{\partial\{u\}} \tag{4.24}$$

with

$$\{x_s\} = \{x_{s0}\} + \{u\} \tag{4.25}$$

$$\{x_e\} = \{x_{e0}\} + \{w\} \tag{4.26}$$

where $\{x_{s0}\}$represents the original coordinates of the structural nodes and $\{x_{e0}\}$ represents the original coordinates of the structural nodes, which are both constant. Therefore

$$\frac{\partial\{x_s\}}{\partial\{u\}} = [I]. \tag{4.27}$$

For $\frac{\partial\{x_e\}}{\partial\{u\}}$, we recall the structured remeshing scheme, in which a fictitious linear elastic problem is solved. The resulting linear system of equations from (4.3) is partitioned in the usual manner, in order to apply the known displacement boundary conditions. In this case, the displacements are known all along the interface with the structural mesh, and unknown in the interior of the electrical mesh. This is expressed in matrix form as:

$$\begin{bmatrix} K_{f_{ss}} & K_{f_{se}} \\ K_{f_{es}} & K_{f_{ee}} \end{bmatrix} \begin{Bmatrix} \{w_s\} \\ \{w_e\} \end{Bmatrix} = \begin{Bmatrix} \{g\} \\ \{0\} \end{Bmatrix}, \tag{4.28}$$

where the electrical mesh displacement is partitioned into those nodes which are on the common interface with the structure ($\{w_s\}$), and those nodes that are not common to the structural mesh ($\{w_e\}$). No external loads are applied on the fictitious elastic domain, hence the external applied loads are zero. The reaction forces at the electrical/structural interface, denoted $\{g\}$ in (4.28), is not required in any subsequent calculations, and therefore never computed.

Note that $\{w_s\} = \{u_b\}$, where $\{u_b\}$ is the displacements of the structure on the common interface. Therefore, once $\{u_b\}$ is known, the new configuration of the electrostatic mesh can be found. $\{w_e\}$ is the unknown displacement of the electrostatic mesh, which depends on $\{w_s\}$.

By solving (4.28), we get

$$\{w_e\} = -[K_{f_{ee}}^{-1}][K_{f_{es}}]\{w_s\} = -[K_{f_{ee}}^{-1}][K_{f_{es}}]\{u_b\} \tag{4.29}$$

Since $\{x_e\} = [\{x_{e_s}\}, \{x_{e_e}\}]^T$, (4.26) can now be split into the two equations

$$\{x_{e_s}\} = \{x_{e0_s}\} + \{w_s\} \tag{4.30}$$
$$\{x_{e_e}\} = \{x_{e0_e}\} + \{w_e\}. \tag{4.31}$$

Therefore the derivative of the coordinates of the nodes in the electrostatic mesh with respect to the structural displacement can be found as

$$\frac{\partial\{x_e\}}{\partial\{u\}} = \left[\frac{\partial\{x_{e_e}\}}{\partial\{u_b\}}, \frac{\partial\{x_{e_s}\}}{\partial\{u_b\}}\right] = [-K_{f_{ee}}^{-1}K_{f_{es}}, I] \tag{4.32}$$

Now, with all the derivative terms expressed analytically, the gradient of the structural residual with respect to displacement, $\frac{\partial \boldsymbol{R_s}}{\partial \boldsymbol{u}}$, can be computed.

The gradient of the structural residual with respect to voltage

Direct differentiation of (4.1) w.r.t. voltage gives

$$\frac{\partial \boldsymbol{R}_s}{\partial \boldsymbol{V}} = -\frac{\partial \boldsymbol{f}_{\text{ext}}}{\partial \boldsymbol{V}}. \tag{4.33}$$

Recall that each element along the structural/electrical interface contributes to the force $\boldsymbol{f}_{\text{ext}}$. Similarly, the above gradient is simply assembled from these element contributions.

From (4.10) and (4.15) it follows that

$$\frac{\partial\{f_{\text{ext}}\}}{\partial\{V\}} = [M]\frac{\partial[T_e]}{\partial\{V\}}\{n\} \tag{4.34}$$

Application of the chain rule to (4.9) gives

$$\frac{\partial[T_e]}{\partial\{V\}} = \frac{\partial[T_e]}{\partial\{e\}}\frac{\partial\{e\}}{\partial\{V\}} = \frac{\partial[T_e]}{\partial e_x} \otimes \frac{\partial e_x}{\partial\{V\}} + \frac{\partial[T_e]}{\partial e_y} \otimes \frac{\partial e_y}{\partial\{V\}}, \tag{4.35}$$

where $\frac{\partial[T_e]}{\partial\{e\}}$ can be found from (4.21). Also, from (4.8) is follows that

$$\frac{\partial\{e\}}{\partial\{V\}} = [B_x]. \tag{4.36}$$

In all cases of interest, two of the four nodal voltages per element are known. Consider the 4 noded electrostatic element that has a common edge with the structural mesh, as shown in Figure 4.2. Notice that the voltage of nodes 2 and 3 is fixed, since the applied voltage on the structure remains constant, and only the voltage of nodes 1 and 4 is allowed to change. Since we are only interested in computing the gradient of the electrostatic force with respect to the *unknown* voltages, only that part of the above computation associated with the two unknown nodal voltages are assembled into the global gradient.

4.3.3 The electrostatic residual

We now provide the details for the computation of the electrostatic residual in (4.2). The permittivity matrix $[K_e]$ is assembled from element contributions, where each element's permittivity matrix is computed as

$$[K_e] = \int_\Omega [B_x]^T \epsilon_0 [B_x] d\Omega. \tag{4.37}$$

As noted before, $[B_x]$ contains the spatial gradients of the voltage interpolation functions, and ϵ_0 is the permittivity of the free space.

In the cases we consider, the charge density $\{q\}$ in the free space is zero, and non-zero at the locations where the voltages are prescribed (see Figure 4.1). Again, we partition the electrostatic residual according to the unknown (subscript u) and known (subscript k) voltages, to obtain the system

$$\begin{bmatrix} K_{e_{kk}} & K_{e_{ku}} \\ K_{e_{uk}} & K_{e_{uu}} \end{bmatrix} \begin{Bmatrix} \{V_k\} \\ \{V_u\} \end{Bmatrix} = \begin{Bmatrix} \{q_k\} \\ \{0\} \end{Bmatrix}. \tag{4.38}$$

Since the charge density at nodes with known voltage (similar to reaction forces in the structural residual) is of no concern, we only consider the electrostatic residual at the nodes of unknown voltage:

$$\{R_e\} = [K_{e_{uk}}]\{V_k\} + [K_{e_{uu}}]\{V_u\} = \{0\}. \tag{4.39}$$

4.3.4 Gradients of the electrostatic residual

Gradient of the electrostatic residual with respect to displacement

Since the electrostatic mesh is updated with the electrostatic mesh displacement after every iteration, the permittivity matrix, which is a function of the nodal coordinates, is no longer a constant. Hence, the gradient of the electrostatic residual with respect to the displacement becomes

$$\begin{aligned} \frac{\partial\{R_e\}}{\partial\{u\}} &= \frac{\partial[K_{e_{uk}}]}{\partial\{u\}}\{V_k\} + \frac{\partial[K_{e_{uu}}]}{\partial\{u\}}\{V_u\} \\ &= \frac{\partial[K_{e_{uk}}]}{\partial\{x_e\}}\frac{\partial\{x_e\}}{\partial\{u\}}\{V_k\} + \frac{\partial[K_{e_{uu}}]}{\partial\{x_e\}}\frac{\partial\{x_e\}}{\partial\{u\}}\{V_u\}. \end{aligned} \tag{4.40}$$

At the element level, numerical integration is used to compute (4.37), and the gradient $\frac{\partial[K_e]}{\partial\{x\}}$ is found as

$$\frac{\partial[K_e]}{\partial\{x_e\}} = \sum_{GP}\left(\frac{\partial[B_e]^T}{\partial\{x_e\}}\epsilon_0[B_e]\det(\boldsymbol{j}) + [B_e]^T\epsilon_0\frac{\partial[B_e]}{\partial\{x_e\}}\det(\boldsymbol{j}) + [B_e]^T\epsilon_0[B_e]\frac{\partial\det(\boldsymbol{j})}{\partial\{x_e\}}\right)W_{GP}. \tag{4.41}$$

In the above, we explicitly indicate summation over the number of Gauss points GP, and $\boldsymbol{j}$ refers to the element Jacobian. The term $\frac{\partial\{x_e\}}{\partial\{u\}}$ is the same as described in (4.32) and the gradient of the determation of Jacobian $\frac{\partial\det(\boldsymbol{j})}{\partial\{x_e\}}$ is given in Appendix B.

Gradient of electrostatic residual with respect to voltage

From (4.39), the gradient is found to be

$$\frac{\partial\{R_e\}}{\partial\{V_u\}} = [K_{e_{uu}}] \tag{4.42}$$

4.3.5 Remark

All four gradients involved in (4.5) are derived analytically, to ensure that the Newton's method can be implemented effectively and efficiently. Note however that the elemental integrations are done numerically; this is efficient, and prevents cumbersome derivations for distorted elements.

4.4 Introduction to other algorithms

Besides Newton's method with analytical gradients, as derived in the foregoing, there are a few other methods or algorithms can may be used to solve our nonlinear coupled system. We will now compare them with the Newton-Raphson method, using the analytical gradients.

4.4.1 Relaxation scheme

A simple black-box approach for the coupled electromechanical analysis is the Gauss-Seidel relaxation algorithm [51]. This scheme is a simple gradient free iterative method that repeatedly calculates the residuals back and forth, until a converged solution is obtained. Due to the simplicity of the scheme, it can be implemented quickly and easily to solve coupled problems.

However, as we will show in the results later, this method requires a large number of iterations to converge when the coupling between the two fields is 'strong'. The method may even fail to converge in the vicinity of the pull-in stage, e.g. see Reference [45]. This scheme makes use of the following update equations:

$$\boldsymbol{V}^i = \boldsymbol{R}_e(\boldsymbol{u}^k) \tag{4.43}$$

$$\boldsymbol{u}^{k+1} = \boldsymbol{R}_s(V^i) \tag{4.44}$$

4.4.2 Newton's method using finite difference gradients

Instead of using analytical gradients, the finite difference method can also be used to generate approximate gradients. But, it is clear that the computational cost is increased significantly, since many more function evaluations are needed.

Additionally, finite difference gradients are approximate, and the sensitivities of the residual depend on the size of the perturbation used in the approximation. In the comparison in this chapter, the forward finite different method is used:

$$\frac{\partial \boldsymbol{R}}{\partial \boldsymbol{u}} = \frac{\boldsymbol{R}(\boldsymbol{u} + \Delta\boldsymbol{u}) - \boldsymbol{R}(\boldsymbol{u})}{\Delta\boldsymbol{u}} \tag{4.45}$$

4.4.3 Nested Newton iteration

Instead of solving both independent variables $\boldsymbol{u}$ and $\boldsymbol{V}$ simultaneously, we may choose to regard one of the independent variables as a function of the other. This results in a Newton's method that has two nested iterative loops, one for each of the variables, as described in [52]. This method can be beneficial if one of the variables has significantly more degrees of freedom than the other. The outer loop, which is iterated fewer times, is used to compute the system with more degrees of freedom, while the inner loop, which is iterated more times, computes the system with fewer degrees of freedom. An example being a structural mesh that has many more degrees of freedom than an air space mesh; this is in fact often the case.

We therefore choose to solve the structural displacement in the outer loop. The voltage is now no longer an independent variable, but a function of the displacement, i.e. $\boldsymbol{V} = \boldsymbol{V}(\boldsymbol{u})$. The structural residual is again solved using Newton's method:

$$\left[\frac{\partial \boldsymbol{R}_s}{\partial \boldsymbol{u}}(\boldsymbol{u}^i, \boldsymbol{V}(\boldsymbol{u}^i)) + \frac{\partial \boldsymbol{R}_s}{\partial \boldsymbol{V}}(\boldsymbol{u}^i, \boldsymbol{V}(\boldsymbol{u}^i))\frac{\mathrm{d}\boldsymbol{V}}{\mathrm{d}\boldsymbol{u}}(\boldsymbol{u}^i)\right]\Delta\boldsymbol{u} = -\boldsymbol{R}_s(\boldsymbol{u}^i, \boldsymbol{V}(\boldsymbol{u}^i)). \tag{4.46}$$

The calculation of $\boldsymbol{V}(\boldsymbol{u})^i$ is performed in the inner loop by solving the electrostatic residual equation using the Newton-Raphson method (with the current displacement $\boldsymbol{u}^i$ fixed):

$$\frac{\partial \boldsymbol{R}_e}{\partial \boldsymbol{V}}(\boldsymbol{u}^i, \boldsymbol{V}^j(\boldsymbol{u}^i))\Delta\boldsymbol{V} = -\boldsymbol{R}_e(\boldsymbol{u}^i, \boldsymbol{V}^j(\boldsymbol{u}^i)) \tag{4.47}$$

$$\boldsymbol{V}^{j+1}(\boldsymbol{u}^i) = \boldsymbol{V}^j(\boldsymbol{u}^i) + \Delta\boldsymbol{V}. \tag{4.48}$$

In the general case, the above subiterations are repeated in the inner loop until a converged solution of $\boldsymbol{V}(\boldsymbol{u}^i)$ is reached. However, for our coupled system, the electrical residual $\boldsymbol{R}_e$ is a linear function of the voltage $\boldsymbol{V}$. Furthermore, the gradient of the electrical residual with respect to the voltage, given by (4.42), is only a function of $\boldsymbol{u}$. Hence, (4.47) is a linear function in $\boldsymbol{V}$ and the exact solution is obtained in a single iteration.

Once $\boldsymbol{V}(\boldsymbol{u}^i)$ is determined, the derivative $\frac{\mathrm{d}\boldsymbol{V}}{\mathrm{d}\boldsymbol{u}}(\boldsymbol{u}^i)$ is obtained by differentiating the electrostatic residual equation:

$$\frac{\partial \boldsymbol{R}_e}{\partial \boldsymbol{u}}(\boldsymbol{u}^i, \boldsymbol{V}(\boldsymbol{u}^i)) + \frac{\partial \boldsymbol{R}_e}{\partial \boldsymbol{V}}(\boldsymbol{u}^i, \boldsymbol{V}(\boldsymbol{u}^i))\frac{\mathrm{d}\boldsymbol{V}}{\mathrm{d}\boldsymbol{u}}(\boldsymbol{u}^i) = \boldsymbol{0} \tag{4.49}$$

$\frac{\mathrm{d}\boldsymbol{V}}{\mathrm{d}\boldsymbol{u}}(\boldsymbol{u}^i)$ is solved from the linear system of equations:

$$\frac{\partial \boldsymbol{R}_e}{\partial \boldsymbol{V}}(\boldsymbol{u}^i, \boldsymbol{V}(\boldsymbol{u}^i))\frac{\mathrm{d}\boldsymbol{V}}{\mathrm{d}\boldsymbol{u}}(\boldsymbol{u}^i) = -\frac{\partial \boldsymbol{R}_e}{\partial \boldsymbol{u}}(\boldsymbol{u}^i, \boldsymbol{V}(\boldsymbol{u}^i)), \tag{4.50}$$

where the matrix $\frac{\partial \boldsymbol{R}_e}{\partial \boldsymbol{V}}$ is already available in factored form, since this is required to solve the linear system in (4.47).

Once $\boldsymbol{V}(\boldsymbol{u}^i)$ and $\frac{\mathrm{d}\boldsymbol{V}}{\mathrm{d}\boldsymbol{u}}(\boldsymbol{u}^i)$ are computed, the process proceeds to the outer loop. The Newton step for the outer loop is computed from (4.46), while the displacement is updated from

$$\boldsymbol{u}^{i+1} = \boldsymbol{u}^i + \Delta\boldsymbol{u}. \tag{4.51}$$

Note that the nested Newton-Raphson method requires no additional gradients as compared to the traditional method. The gradients $\frac{\partial \boldsymbol{R}_s}{\partial \boldsymbol{u}}$ and $\frac{\partial \boldsymbol{R}_s}{\partial \boldsymbol{V}}$ in (4.46), and the gradients $\frac{\partial \boldsymbol{R}_e}{\partial \boldsymbol{u}}$ and $\frac{\partial \boldsymbol{R}_e}{\partial \boldsymbol{V}}$ in (4.50) are all required in the traditional method, and their calculation have been discussed in the previous sections.

4.5 Numerical results

The foregoing formulation was implemented in Matlab [53]. Although not computationally efficient, development time is minimized and comparisons can be made between alternative solution strategies. All simulations were performed on a Pentium P4 2.8GHz CPU with 512 RAM personal computer.

4.5.1 Geometrically linear analysis

For the geometrically linear coupled analysis, a cantilever beam over ground example is presented here. The beam length is 500 μm and the width is 14.35 μm, while the bottom air gap is 1 μm. Young's modulus E is taken as 169 GPa, and Poisson's ratio ν is set to 0.3. The only boundary conditions for the electrostatic problem is the non-zero prescribed voltage for the beam surface, and the zero prescribed voltage for the bottom electrode. It was verified numerically that the length of the bottom electrode (chosen as 550 μm), and the size of the air gap at the top of the beam (chosen as 1 μm) does not affect the results.

Numerical verification of gradients

In order to numerically verify that all the gradient calculations are correct, the norm of the total system residual, displacement update vector and voltage update vector is summarized in Table 4.1. This particular problem was analyzed with an uniform beam mesh of 280×8 elements, and 8 through-thickness elements was used to model both the bottom and top air gaps. The applied beam voltage is 16 V. It is evident from the values in Table 4.1 that quadratic convergence is obtained, a good indication that the analytical gradients were correctly derived and implemented.

Iteration #	$\|\boldsymbol{R}_i\|/\|\boldsymbol{R}_1\|$	$\|\Delta \boldsymbol{u}\|$	$\|\Delta \boldsymbol{V}\|$
1	1.0000	6.6012	5.2615×10^{-1}
2	1.0926×10^{-1}	1.2873	3.1181×10^{-1}
3	8.9703×10^{-3}	1.1951×10^{-1}	2.4498×10^{-2}
4	1.3141×10^{-4}	1.0860×10^{-3}	2.3049×10^{-4}
5	9.2402×10^{-7}	1.3986×10^{-6}	1.8556×10^{-7}

Table 4.1: Convergence history for geometrically linear coupled problem

Mesh refinement study

To illustrate that the solution to the coupled problem converges, a mesh refinement study is performed. The above problem is solved for a series of meshes. The beam tip vertical displacement is summarized in Table 4.2, for an applied beam voltage of 16 V. To depict the mesh clearly, a coarse mesh is shown in Figure 4.4. (This figure is not drawn to scale.)

Beam mesh	# Layers per air gap	Vertical displacement
70×2	2	-0.314306
140×4	4	-0.314975
280×8	8	-0.315628

Table 4.2: Beam tip vertical displacement versus mesh refinement.

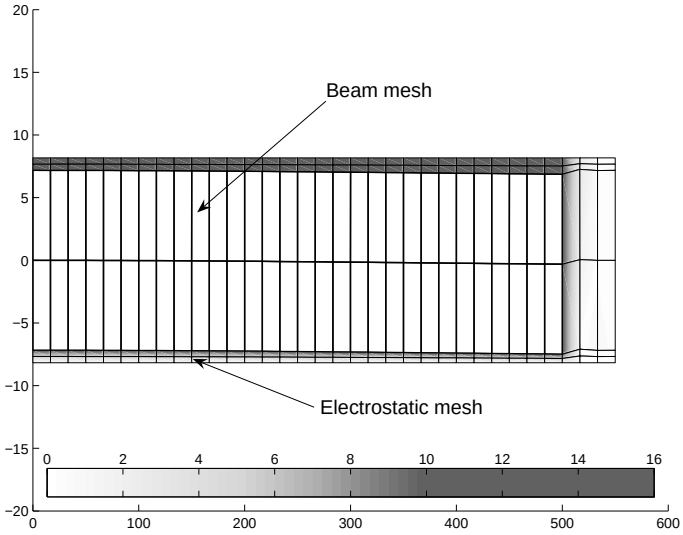

Figure 4.4: Coarse deformed mesh of the system (not drawn to scale). The beam mesh uses 30×2 elements, and 2 through-thickness elements are used for both air gaps. Grayscale contours represent the voltage values in the electrostatic mesh.

Tip deflection

Now that the numerical implementation of the formulation has been verified, the code is used to compute the voltage-deflection characteristic of the device. For all results in this section, a 140×4 beam mesh and a 4 layer air mesh for both gaps are used.

According to [54], the pull-in voltage for a cantilever beam is approximately calculated as

$$V_{PI} = \sqrt{\frac{8K_{\text{eff}}d_0^3}{18.2\varepsilon_0 l b_{\text{eff}}}} \tag{4.52}$$

with

$$K_{\text{eff}} = \frac{2}{3}\frac{Ebh^3}{l^3}\frac{3}{8 - 6\lambda_r + \lambda_r^3} \tag{4.53}$$

and

$$b_{\text{eff}} = b\left(1 + 0.65\frac{(1-\beta)d_0}{b}\right). \tag{4.54}$$

The loading factor $\lambda_r = 1$, b is the width of the beam, d_0 is the initial gap between the beam and the electrode, l is the length of the beam, h is the height of the beam, β is the normalized maximum

deflection of the beam and is suggested to be 0.45 for this cantilever beam. The analytical pull-in voltage is calculated to be 16.2 volt.

As shown in Figure 4.5, 16.2 volt falls almost exactly between the deflection curves of plane strain and plane stress calculated using Newton's method with analytical gradients. This is to be expected, since the actual 3-D beam will be softer then the 2-D plane strain beam, but harder than the 2-D plane stress beam. The numerical values of the vertical tip deflection can be found in Table 4.3.

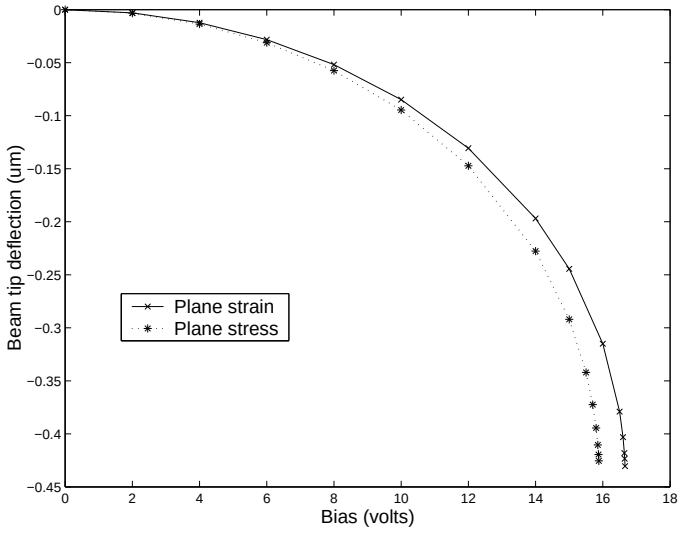

Figure 4.5: Tip deflection of the beam.

Plane strain		Plane stress	
Bias (Volts)	Deflection (μm)	Bias (Volts)	Deflection (μm)
2	-0.003036	2	-0.00334
4	-0.012292	4	-0.013542
6	-0.028254	6	-0.031197
8	-0.051869	8	-0.057490
10	-0.084873	10	-0.094656
12	-0.130622	12	-0.147298
14	-0.196931	14	-0.227699
15	-0.244411	15	-0.291988
16	-0.314975	15.5	-0.342088
16.5	-0.379054	15.7	-0.372452
16.6	-0.403065	15.8	-0.394450
16.64	-0.418137	15.85	-0.410437
16.65	-0.423444	15.87	-0.419455
16.66	-0.430464	15.88	-0.425402

Table 4.3: Tip deflection for plane strain and plane stress conditions

Comparison with the relaxation method

The performance of the relaxation and Newton algorithms is summarized in Table 4.4. It is noticed that the Newton algorithm takes fewer iterations and is much faster than the relaxation algorithm for the tightly coupled cases (i.e. near the pull-in voltage). To further highlight the sensitivity of the relaxation method near the pull-in voltage, Figure 4.6 depicts the residual norm convergence for an applied voltage of 16.65 V and 16.66 V, which results in an iteration increase form 74 to 95.

Bias (volts)	CPU (s)		Number of iterations	
	Relaxation	Newton	Relaxation	Newton
2	16.7	46.9	3	2
4	17.0	49.3	3	2
6	22.3	68.7	4	3
8	27.9	69.6	5	3
10	33.2	68.4	6	3
12	33.5	68.9	7	3
14	55.2	91.2	10	4
15	75.8	91.4	12	4
16	107.0	114.9	19	5
16.5	185.1	137.8	33	6
16.6	255.4	148.4	46	6
16.64	368.6	137.2	64	6
16.65	401.1	160.4	74	7
16.66	528.4	160.5	95	7

Table 4.4: Comparison of relaxation and Newton algorithm based on the number of iterations to convergence, and total CPU time.

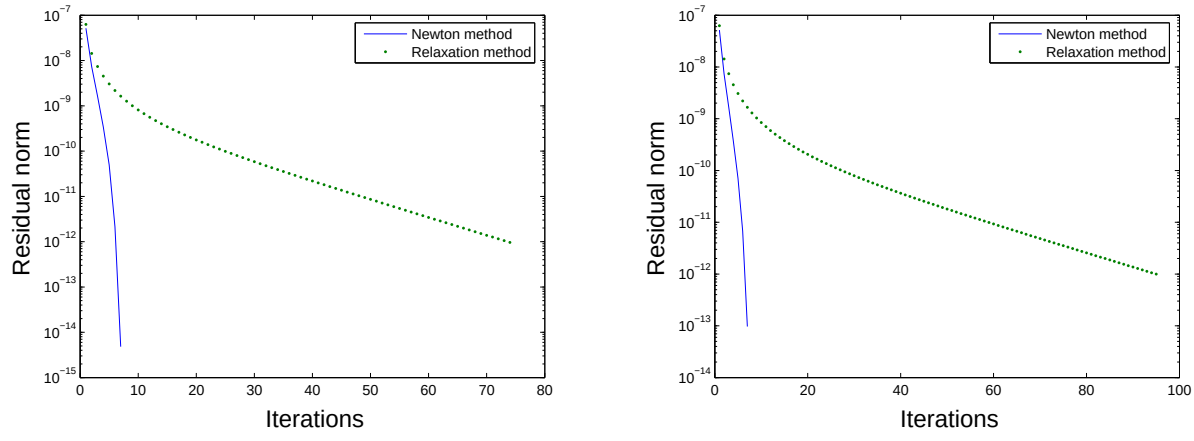

(a) (b)

Figure 4.6: Convergence of the residual norm for both the relaxation and Newton algorithms, with an applied bias of (a) 16.65 V and (b) 16.66 V.

Comparison with nested Newton's method

The advantage of the nested Newton's method is shown in Table 4.5. As the beam mesh degrees of freedom increase, while the air mesh degrees of freedom remain relatively unchanged, the computational time is significantly reduced when using the nested Newton's method. This is important, since accuracy considerations require a refined beam mesh, while the air mesh can be left relatively coarse.

Number of degrees of freedom		CPU (s)	
Beam	Air	Single iteration	Nested iteration
1410	1595	114.9	120.9
2898	1889	190.5	158.9
4706	1403	156.4	135.2
6432	1300	463.7	144.4
7258	1255	596.3	142.2
8442	1725	884.2	206.0

Table 4.5: Comparison of CPU times for a single Newton iteration and a nested Newton iteration algorithm with an applied bias of 16 V

Comparison with finite difference gradient

The computational time increases significantly as the number of system degrees of freedom increase when finite differences are used to approximate the gradients, since the number of required system residual evaluations is proportional to the number of degrees of freedom. Table 4.6 shows the comparison between CPU times required by Newton's method using the analytical gradient, compared to Newton's method using finite difference gradients.

Number of degree of freedom	CPU (s)	
	Finite difference gradient	Analytical gradient
267	17.8	5.3
394	386.5	7.83
760	1677.7	16.5
1058	3345.1	23.7

Table 4.6: Comparison of CPU times for analytical gradients and finite difference gradients with an applied bias of 10 V.

4.5.2 Geometrically nonlinear analysis

A typical application of geometrically nonlinear beams is large stroke actuators, in which the beams are stiffened due to large deflection, and fixed-fixed beam devices (clamped membranes), in which the beam starts to behave nonlinearly at very small displacements due to large axial stresses [55]. In both cases, geometric nonlinear effects have to be taken into account during simulations.

Geometrically nonlinear cantilever microbeam simulations often require unstructured remeshing, since the elements are distorted due to the large deflection, as shown in Figure 4.7. (The dimensions of this beam are the same as the one used in Reference [47], and are outside the scope of this thesis. However, some numerical results for the large deflection of a cantilever beam can be found in [47].) Note that during Newton iterations of a nonlinear system, the sign of the determinant of the element Jacobian, $\det(\boldsymbol{J})$, is checked. A negative $\det(\boldsymbol{J})$ is an indication of element inversion; this requires a reduction in the Newton step size.

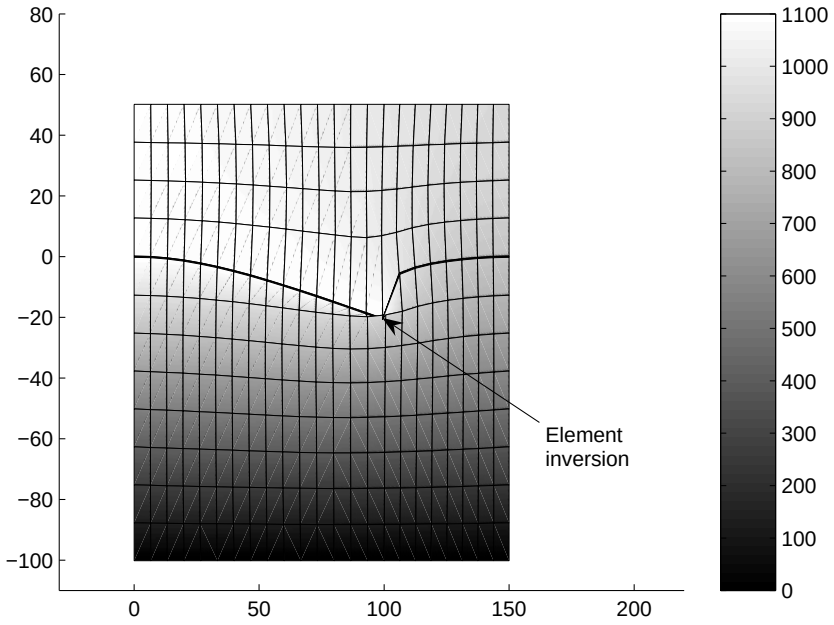

Figure 4.7: Deformation of the cantilever beam and the mesh. The grayscale contours represent the nodal voltages in the electrostatic mesh.

A fixed-fixed beam is now selected to illustrate the effect of geometric nonlinearity in coupled electro-mechanical systems. The fixed-fixed beam is also widely used in MEMS, as shown in Figure 4.8 and Figure 4.9. The geometrically nonlinear mixed assumed stress element described in the previous chapter is used to model the beam, and analytical gradients are again used when solving the coupled system.

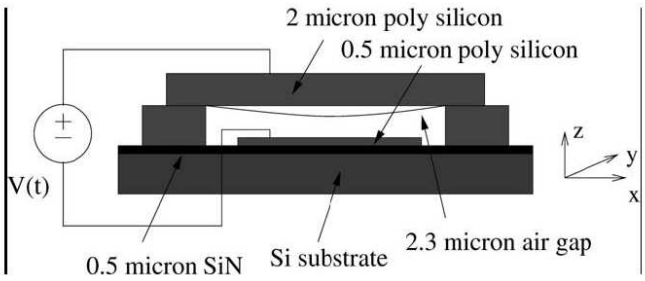

Figure 4.8: Schematic views of fixed-fixed beam microstructure used as pressure sensor [56].

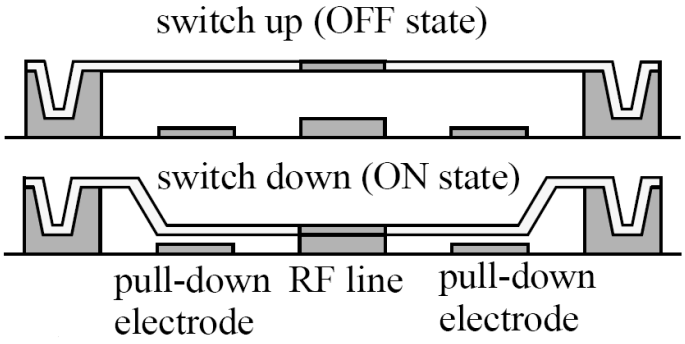

Figure 4.9: Basic structure of RF switch [57, 58].

Theoretical example: beam number 1

The major difference between linear and nonlinear models can be seen clearly as the deflection of the beam increases, which requires a high applied bias. In order to show the ability of the proposed element and the algorithm in modeling a geometrically nonlinear electrostatic-mechanical coupled system, an unrealistic high voltage is applied to take the system deep into its nonlinear zone. In this example, the beam is of unit height, while the length is 100 μm. The gap between the beam and the electrode is 100 μm; the material parameters are $E = 70$ GPa and $\nu = 0.3$. The beam mesh is discretized with a 2×20 mesh, using plane stress conditions. The air mesh, which models the bottom air gap, has 4 layers. No top air gap is present.

In Figure 4.10, the deformations of the beam for both a linear and a nonlinear analysis are shown. It is found that the linear beam deforms much more than the nonlinear beam, even when the applied bias is relatively low.

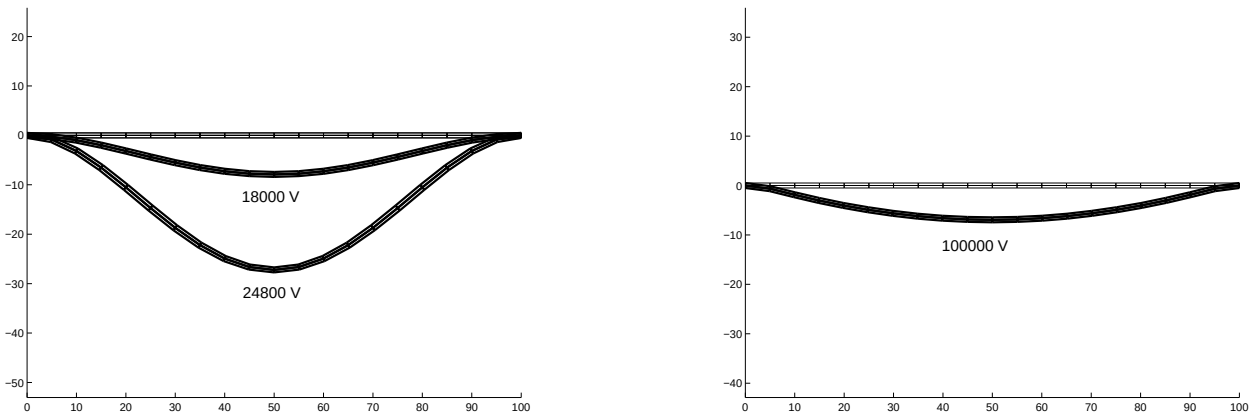

(a) (b)

Figure 4.10: Deformation of beam number 1, using a geometrically (a) linear and (b) nonlinear formulation.

Also clearly shown in Table 4.7 and Figure 4.11 is that nonlinear stiffening contributes significantly from the early stages of deformation. It is noted that the linear model cannot handle high

applied voltages, as this passes the model's pull-in limit, while the stiffened nonlinear model can accommodate much higher voltage loads.

Bias (volts)	Deflection	
	Linear	Nonlinear
1000	-0.01945	-0.01944
2000	-0.07792	-0.07758
4000	-0.3137	-0.2951
8000	-1.289	-0.8442
16000	-5.885	-1.704
18000	-7.907	-1.885
20000	-10.574	-2.058
22000	-14.358	-2.223
24000	-20.957	-2.383
24800	-27.232	-2.446
50000		-4.161
100000		-6.941

Table 4.7: Beam number 1 deflection versus applied bias for both geometrically linear and nonlinear cases.

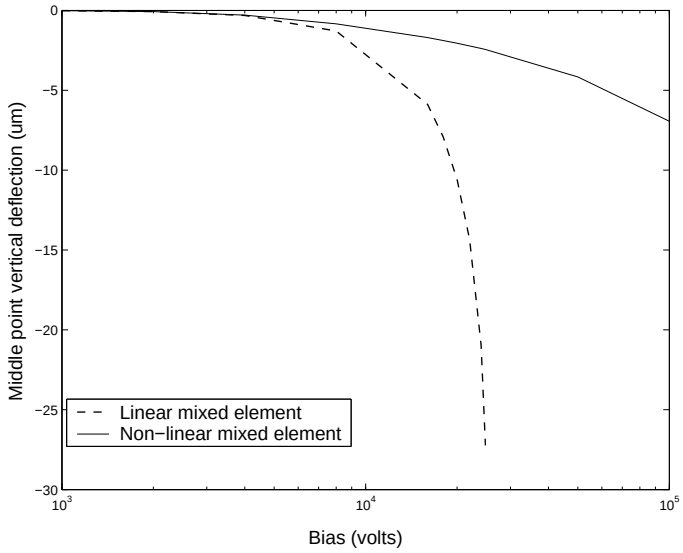

Figure 4.11: Load-deflection curve of beam number 1 for geometrically linear and nonlinear analysis.

In order to study the convergence of the method, a mesh refinement convergence test is performed. The result shows that the displacement converges as the number of degrees of freedom increases, as depicted in Figure 4.12.

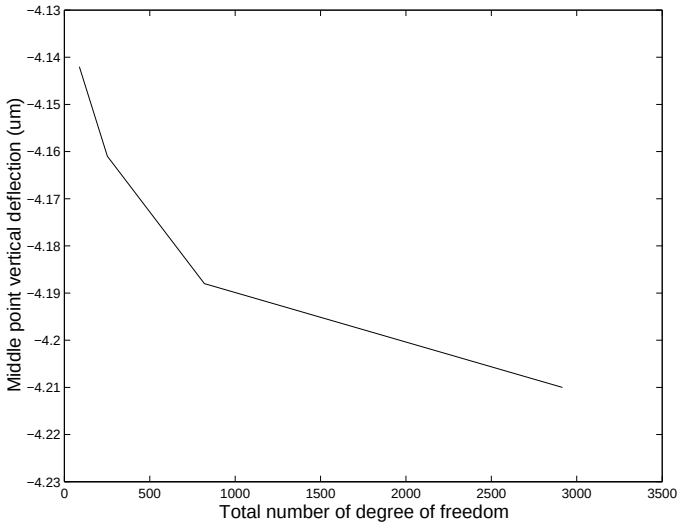

Figure 4.12: Convergence of the midpoint vertical displacement, for beam number 1.

Realistic example: beam number 2

The same beam as in the previous example is now studied, but the gap is reduced to 10 μm. The beam mesh is 8×80 and the air mesh has 16 layers.

As is clearly shown in Table 4.8 and Figure 4.13, nonlinear stiffening delays the pull-in stage significantly. When the linear model starts to get to the highly nonlinear pull-in zone at around 960 V, the geometrically nonlinear model, which undergoes axial stress stiffening, is still well within its nearly linear responding zone.

Bias (volts)	Deflection	
	Linear	Nonlinear
100	-0.0195	-0.0195
200	-0.07874	-0.07839
400	-0.328	-0.3062
600	-0.7986	-0.6109
800	-1.655	-0.9109
850	-1.994	-0.9824
900	-2.447	-1.052
950	-3.226	-1.121
960	-3.562	-1.135

Table 4.8: Beam number 2 deflection versus loads for both linear and nonlinear cases.

A mesh refinement convergence test is again performed, and the result shows that the displacement converges as the number of degrees of freedom increases (Figure 4.14). The deformed shape of an intermediate mesh (4×40), together with the deformed electrostatic mesh (4×40), is shown in Figure 4.15.

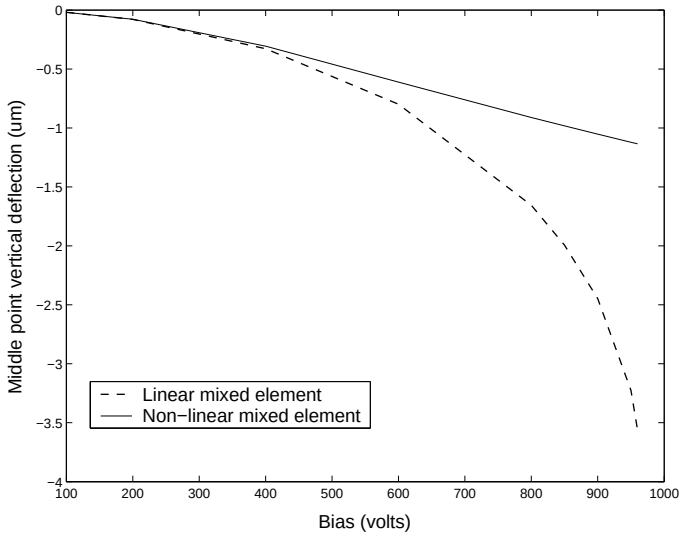

Figure 4.13: Load-deflection curve of beam number 2 for linear and nonlinear analysis.

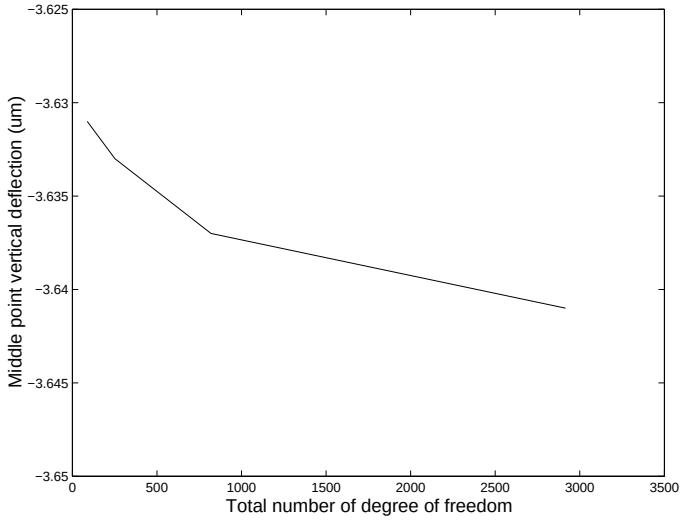

Figure 4.14: Fixed-fixed beam number 2 problem: Convergence of the middle point vertical displacement.

4.6 Conclusions

In this chapter, Newton's method with analytically derived gradients was used to solve an electromechanically coupled system. It was shown that Newton's method with analytical gradients converges very rapidly, even for the tightly coupled stage between the mechanical and electrical domains. In this strongly coupled regime, the number of iterations required for convergence is an order less for Newton's method, as compared to the relaxation scheme. With a nested Newton method, the computational process can be even more efficient. The computational time is also significantly reduced through the use of analytical gradients rather than finite difference gradients. When geometrically nonlinear mixed assumed stress elements are used to model the structure, the

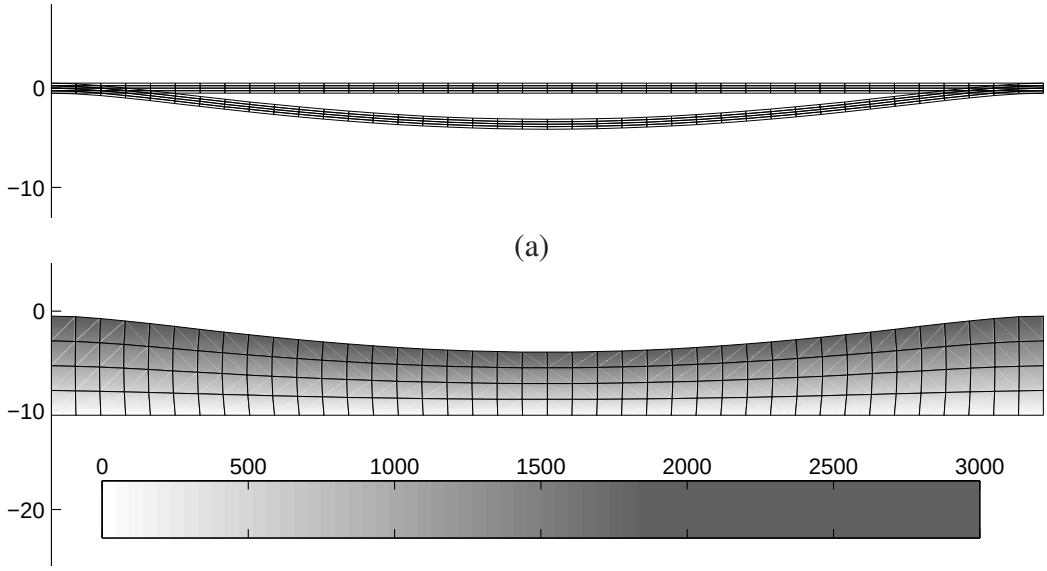

Figure 4.15: (a) Original and deformed structural mesh and (b) deformed electrostatic mesh of beam number 2, subjected to a bias of 3000 V. The grayscale contours in (b) represent the voltages.

geometric nonlinearity of the coupled system can be well modeled and analyzed using the same analytical gradients. Newton's method with analytically derived gradients can be extended and modified for 3-D or other coupled fields in MEMS.

Chapter 5

Conclusions and Recommendations

5.1 General remarks

In this thesis, some fundamental issues involved in the simulation and analysis of MEMS were studied, which are two critical aspects when designing MEMS: the effect of element formulation (type), and the effects of the algorithm used to solve the system of coupled MEMS equations.

In order to accurately model and predict the characteristics of an electrostatic-mechanical coupled system, a geometrically nonlinear version of the popular 5β assumed stress element was proposed. After construction of the FEM model with this nonlinear mixed element, the coupled residuals are solved using Newton's method, which in turn uses analytical gradients.

5.2 Conclusions

The following conclusions are drawn from this study:

1. FEM is still an effective method to analyze the behavior of MEMS, if elements of adequate accuracy are used.
2. The geometrically nonlinear mixed assumed stress element proposed for use in MEMS is consistent and rank sufficient.
3. The element uses only linear interpolation fields for the elemental displacement fields, with only four nodes per element.
4. In the absence of follower loads, the consistent tangent for the geometrically nonlinear system is symmetric, which allows it to be solved very efficiently.
5. In the presence of singularities, the accuracy of the proposed nonlinear mixed element is comparable to the well-known Q8 element.
6. Although inversion of the partition matrix is required for the proposed element, the matrix remains constant and it can therefore be computed efficiently.

7. Numerical results confirm that the element is an attractive choice for geometrically nonlinear analyses, when reducing the computational cost and accuracy are both important.

8. The quadratic convergence rate of the Newton-Raphson algorithm makes it an attractive method for solving the nonlinear system of equations obtained when modeling the electrostatic-mechanical coupled system with FEM.

9. The derived analytical gradients significantly reduce the computational cost, since the most critical and costly step in the Newton iteration is the gradient evaluation process.

10. The accurate analytical gradients derived ensure rapid convergence of Newton's method, as demonstrated using numerical results.

5.3 Recommendations for future work

A few recommendations are made for future consideration:

1. Other meshless modeling techniques such as the finite cloud method (FCM) and the boundary cloud method (BCM) [59, 60] may be studied as a comparison with the traditional FEM modeling.

2. Other algorithmic options, such as a multilevel Newton method [45, 61] for solving nonlinear system of equations can be studied. (Computational cost and convergence rate are the two most important criteria for evaluation.)

3. Since the frequency response is an important design parameter in some MEMS, dynamic modeling may be developed.

4. Both the geometrically nonlinear mixed assumed stress element and the analytical gradients developed could be extended to 3-D modeling.

5. A more robust method of developing the analytical gradient should be proposed so that it can be easily extended to solve other mixed domain systems.

6. A completely unstructured remeshing scheme could be used in association with the proposed element for analyzing large deformation problems.

7. A comparative study can be done regarding the choice of different interpolations in the assumed stress interpolation matrix P of the proposed nonlinear element.

Bibliography

[1] Danny Bank. *Microengineering, MEMS, and Interfacing*. CRC, March 2006.

[2] H. M Newman. *Direct Digital Control of Building Systems*. John Wiley and Sons, 1994.

[3] J. W. Gardner. *Microsensors*. John Wiley and Sons, 1994.

[4] W. Tang, T. Nguyen, and R. Howe. Laterally driven polysilicon resonant microstructures. *Institute of Electrical and Electronic Engineers: microelectromechanical systems*, pages 53–59, 1989.

[5] J.R. Gilbert, R. Legtenberg, and S.D. Senturia. 3D coupled electro-mechanics for MEMS: Applications of CoSolve-EM. *Institute of Electrical and Electronic Engineers: microelectromechanical systems*, pages 122–27, 1995.

[6] M. Daneshmand. *Multi-Port RF MEMS Switches and Switch Matrices*. PhD thesis, University of Waterloo, 2006.

[7] E.R. Brown. Rf-MEMS switches for reconfigurable integrated circuits. *Institute of Electrical and Electronic Engineers: Transactions on Microwave Theory and Techniques*, 46(11), 1998.

[8] Q. Jing, T. Mukherjee, and G. K. Fedder. Large-deflection beam model for schematic-based behavioral simulation in nodas. *Technical Proceedings of the 2002 International Conference on Modeling and Simulation of Microsystems*, 1:136–139, 2002.

[9] *Market Analysis for Microsystems 2000-2005*, February 2002.

[10] F. Chollet and Haobing Liu. A not so short introduction to micro electromechanical systems. Unpublished document on the internet, 2006.

[11] F. Berry and M. A. Kriss. Electronic imaging. *SPIE International Technical Group Newsletter*, 14, 2004.

[12] J. Chen, S. Kang, J. Zou, and Liu C. Reduced-order modeling of weakly nonlinear MEMS devices with Taylor-series expansion and Arnoldi approach. *Journal of Microelectromechanical Systems*, 13(3), June 2004.

[13] M. Madou. *Fundamentals of Microfabrication*. Chemical Rubber Company Press, Boca Raton, FL, 2nd edition, 2002.

[14] B. Choi and G. Lovell, E. Improved analysis of microbeams under mechanical and electrostatic loads. *Journal of Micromechanics and Microengineering*, pages 724–729, 1997.

[15] M. Gyimesi and D. Ostergaard. Electro-mechanical transducers for MEMS analysis in Ansys. *Proceedings of MSM Conference (Puerto Rico)*, pages 270–273, 1999.

[16] J. G. Michopoulos, C. Farhat, and J. Fish. Modeling and simulation of multiphysics system. *Journal of Computing and Information Science in Engineering*, 5:198–213, 2005.

[17] T-R. Hsu. *MEMS and Microsystems Design and Manufacture*. New York: McGraw-Hill, 2001.

[18] C. Nathanson, H, E. Newell, W, A. Wickstrom, R, and J. R. Davis. The resonant gate transistor. *Institute of Electrical and Electronic Engineers: Transaction on Electron Devices*, 14:117–113, 1967.

[19] P. Raback and A. Pursula. Finite element simulation of the electro-mechanical pull-in phenomenon. *European Congress on Computational Methods in Applied Sciences and Engineering*, July 2004.

[20] P. Osterberg. *Electrostatically Actuated Microelectromechanical Test Structures for Material Property Measurement*. PhD thesis, MIT, September 1995.

[21] N.M. Rensing, S. Dodson, G.G. Adams, P.M. Zavracky, R.W. McClelland, and A. Lemoncelli. Modeling, simulation, and testing of the nonlinear oscillations of a MEMS torsional mirror with mechanical-electrostatic coupling. *Micro-Electro-Mechanical-Systems ASME International Congress and Exposition*, 1:143–50, 1999.

[22] C. Farhar, C. Degand, B. Koobus, and M. Lesoinne. Torsional springs for two-dimensional dynamic unstructured fluid meshes. *Computational Methods of Applied Mechanical Engineering*, 163:231–245, 1998.

[23] K. Maute, M. Nikbay, and C. Farhat. Coupled analytical sensitivity analysis and optimization of three-dimensional nonlinear aeroelastic systems. *American Institute of Aeronautics and Astronautics Journal*, 39(11):2051–2061, 2001.

[24] K. Maute, M. Nikbay, and C. Farhat. Sensitivit y analysis and design optimization of three-dimensional nonlinear aeroelastic systems by the adjoint method. *International Journal of Numerical Methods*, 56(6):911–933, 2003.

[25] M. J. Felton. Gc is in the chips. *Today's Chemist at work*, 11:26–31, 2002.

[26] M. Mehregany. Micro-electro-mechanical systems. *Institute of Electrical and Electronic Engineers: Circuit and Devices*, pages 14–22, July 1993.

[27] W. Bacher, W. Menz, and J. Mohr. The liga technique and its potential for microsystems - a survey. *Institute of Electrical and Electronic Engineers: Transaction on Industrial Electronics*, 42(5), 1995.

[28] J. Bryzek. Impact of MEMS technology on society. *Sensors Actuators*, A 56:1–9, 1996.

[29] *Microelectromechanical Systems Advanced Materials and Fabrication Methods*. Washington, DC, 1997.

[30] N Maluf. *An introduction to microelectromechanical systems engineering*. Artech House, Boston, 2000.

[31] W. Judy, J. Microelectromechanical systems (MEMS): fabrication, design and applications. *Institute of Physics Publishing: Smart Material Structure*, 10:1115–1134, 2001.

[32] H. Pian, T and K. Sumihara. Rational approach for assumed stress finite elements. *International Journal for Numerical Methods in Engineering*, 20:1685–1695, 1984.

[33] S. Atluri. On the hybrid stress finite element model for incremental analysis of large deflection problems. *International Journal of Solids structures*, 9:1177–1191, 1973.

[34] P. L. Boland and T. H. H. Pian. Large deflection analysis of thin elastic structures by the assumed stress hybrid finite element method. *Computer and Structures*, pages 1–12, 1977.

[35] K. Y. Sze and S. J. Zheng. A hybrid stress nine-node degenerated shell element for geometric nonlinear analysis. *Computaional Mechanics*, pages 448–456, 1999.

[36] C. Sansour and F.G. Kollmann. Families of 4-node and 9-node finite element for a finite deformation shell theory. An assesment of hybrid stress, hybrid strain and enhanced strain elements. *Computaional Mechanics*, pages 435–447, 2000.

[37] K. Liu, W, T. Belytschko, and S. Chen, J. Nonlinear versions of flexurally superconvergent elements. *Computer Methods in Applied mechanics and Engineering*, 71:241–258, 1988.

[38] D. Cook, R, S. Malkus, D, E. Plesha, M, and J. Witt, R. *Concepts and Applications of Finite Element Analysis*. John Wiley & Sons, 4th edition, 2002.

[39] E. Gurtin, M. *An Introduction to Continuum Mechanics*. Academic Press, New York, 1981.

[40] E. Tonti. On the mathematical structure of a large class of physical theories. *Accademia Nazionale dei Lincei, estratto dai Rendiconti della Classe di Scienze fisiche, matematiche e naturali*, Serie VIII, Vol. LII(fasc. 1), 1972.

[41] S Di and E. Ramm. On alternative mixed stress 2d and 3d elements. *Engineering Computations*, 11:49–68, 1994.

[42] S. Kok. Numerical solutions for pure flexure of thick 2d beams. *Article under preparation*, 2007.

[43] T. Beléndez, C. Neipp, and A. Beléndez. Large and small deflections of a cantilever beam. *European Journal of Physics*, 23:371–379, 2002.

[44] M. Allen, M. Raulli, K. Maute, and D.M. Frangopol. Reliability-based analysis and design optimization of electrostatically actuated MEMS. *Computers and Structures*, 82:1007–1020, 2004.

[45] N.R. Aluru and J. White. A multilevel Newton method for mixed-energy domain simulation of MEMS. *Journal of Microelectromechanical Systems*, 8(3):299–308, 1999.

[46] P.M. Osterberg and S. Senturia. MTEST: a test chip for electrostatically actuated test structures. *Journal of Microelectromechanical Systems*, pages 107–18, 1997.

[47] R. Gupta. *Electrostatic pull-in test structure design for in-situ mechanical property measurements of microelectromechanical systems (MEMS)*. PhD thesis, Massachussets Insitute of Technology, 1997.

[48] O.C. Zienckiewicz. *The Finite Element Method*, volume 2. New York: McGraw-Hill, Oxford, 4th edition, 1989.

[49] A. Collenz, F.D. Bona, A. Gugliotta, and A. Soma. Large deflection of microbeams under electrostatic loads. *Journal of Micromechanics and Microengineering*, 14:365–373, 2004.

[50] M. Kaltenbacher, S. Reitzinger, and J. Schoeberl. On computational methods for structural reliability analysis. *Institute of Electrical and Electronic Engineers: microelectromechanical systems*, 36:1561–1564, 2000.

[51] X. Cai, H. Yie, P. Osterberg, J. Gilbert, S. Senturia, and J. White. A relaxation/multipole-accelerated scheme for self-consistent electromechanical analysis of complex 3-d microelectromechanical structures. *Proceedings of 11th International Conference of Computer-Aided Design*, pages 283–287, Nov 1993.

[52] P. Michaleris, D.A. Tortorelli, and C.A. Vidal. Tangent operators and design sensitivity formulations for transient non-linear coupled problems with applications to elastoplasticity. *International Journal for Numerical Methods in Engineering*, 37:2471–2499, 1994.

[53] *Matlab User's Guide*. The MathWorks, Inc., 2006.

[54] S. Pamidighantam, R. Puers, K. Baert, and H.A.C. Tilmans. Pull-in voltage analysis of electrostatically actuated beam structures with fixed-fixed and fixed-free end conditions. *Journal of Micromechanics and Microengineering*, 12:458–464, 2002.

[55] G.K. Fedder. *Simulation of Microelectromechanical Systems*. PhD thesis, UC Berkeley, 1994.

[56] R.K. Gipta and S.D. Senturia. Pull-in time dynamics as a measure of absolute pressure. *Institute of Electrical and Electronic Engineers: MEMS*, pages 290–94, 1997.

[57] N. S. Barker and G. M. Rebeiz. Distributed MEMS true-time delay phase shifters and wideband switches. *Institute of Electrical and Electronic Engineers: Transactions on Microwave Theory and Techniques*, 46(11):1881–90, 1998.

[58] G.L. Tan and G.M. Rebeiz. A DC-contact MEMS shunt switch. *Institute of Electrical and Electronic Engineers: Microwave and Wireless Components Letters*, pages 212–14, 2002.

[59] Li. Gang and N.R. Aluru. Efficient mixed-domain analysis of electrostatic MEMS. *Institute of Electrical and Electronic Engineers*, 2002.

[60] Li. Gang and N.R. Aluru. A boundary cloud method with a cloud-by-cloud polynomial basis. *Engineering Analysis with Boundary Elements*, 27:51–71, 2003.

[61] J.Y. Kim, N.R. Aluru, and D.A. Tortorelli. Improved multi-level newton solvers for fully-coupled multi-physics problems. *International Journal for Numerical Methods in Engineering*, 58:463–480, 2003.

Appendix A

Geometrically nonlinear mixed assumed stress element

Computation of the matrices $[B_X]$, $[B_x]$ and the derivative $\frac{d[B_x]}{dU_i}$ are now outlined. For our 4 node quadrilateral element with bilinear interpolation, the shape functions are given by

$$N_1 = \frac{1}{4}(1-\xi)(1-\eta), \tag{A.1}$$

$$N_2 = \frac{1}{4}(1+\xi)(1-\eta), \tag{A.2}$$

$$N_3 = \frac{1}{4}(1+\xi)(1+\eta), \tag{A.3}$$

$$N_4 = \frac{1}{4}(1-\xi)(1+\eta). \tag{A.4}$$

Using the isoparametric formulation, these shape functions are used to interpolate both the displacement field, as well as the geometry i.e.

$$\boldsymbol{u} = [N]\{U\}, \quad \boldsymbol{X} = [N]\{X\}, \quad \text{and} \quad \boldsymbol{x} = [N]\{x\}. \tag{A.5}$$

The element Jacobian $\boldsymbol{J}$ is defined as

$$\boldsymbol{J} = \begin{bmatrix} \frac{dX}{d\xi} & \frac{dY}{d\xi} \\ \frac{dX}{d\eta} & \frac{dY}{d\eta} \end{bmatrix} = \begin{bmatrix} J_{11} & J_{12} \\ J_{21} & J_{22} \end{bmatrix}. \tag{A.6}$$

For an isoparametric formulation, the Jacobian is conveniently computed in vector form $\{J\}$, using the relation

$$\{J\} = \begin{Bmatrix} J_{11} \\ J_{21} \\ J_{12} \\ J_{22} \end{Bmatrix} = [D]\{X\}, \tag{A.7}$$

where the matrix $[D]$ contains the derivatives of the shape functions N w.r.t. natural coordinates ξ and η

$$[D] = \begin{bmatrix} N_{1,\xi} & 0 & N_{2,\xi} & 0 & N_{3,\xi} & 0 & N_{4,\xi} & 0 \\ N_{1,\eta} & 0 & N_{2,\eta} & 0 & N_{3,\eta} & 0 & N_{4,\eta} & 0 \\ 0 & N_{1,\xi} & 0 & N_{2,\xi} & 0 & N_{3,\xi} & 0 & N_{4,\xi} \\ 0 & N_{1,\eta} & 0 & N_{2,\eta} & 0 & N_{3,\eta} & 0 & N_{4,\eta} \end{bmatrix}, \tag{A.8}$$

and the vector $\{X\}$ contains the reference (undeformed) coordinates of the element nodes, i.e.

$$\{X\} = [X_1 \;\; Y_1 \;\; X_2 \;\; Y_2 \;\; X_3 \;\; Y_3 \;\; X_4 \;\; Y_4]^{\mathrm{T}}. \tag{A.9}$$

A simple application of the chain rule of differentiation shows that the Jacobian relates the gradients w.r.t. the natural coordinates to the gradients w.r.t. the reference coordinates :

$$\begin{Bmatrix} \frac{d(\,)}{d\xi} \\ \frac{d(\,)}{d\eta} \end{Bmatrix} = [J] \begin{Bmatrix} \frac{d(\,)}{dX} \\ \frac{d(\,)}{dY} \end{Bmatrix}. \tag{A.10}$$

Hence, the spatial gradients of any quantity interpolated by the shape functions are computed from

$$\begin{Bmatrix} \frac{d(\,)}{dX} \\ \frac{d(\,)}{dY} \end{Bmatrix} = [\Psi] \begin{Bmatrix} \frac{d(\,)}{d\xi} \\ \frac{d(\,)}{d\eta} \end{Bmatrix}, \tag{A.11}$$

where $[\Psi]$ is the inverse of the Jacobian matrix:

$$[\Psi] = \begin{bmatrix} \Psi_{11} & \Psi_{12} \\ \Psi_{21} & \Psi_{22} \end{bmatrix} = [J]^{-1} = \frac{1}{\det(\boldsymbol{J})} \begin{bmatrix} J_{22} & -J_{12} \\ -J_{21} & J_{11} \end{bmatrix}. \tag{A.12}$$

The matrix $[B_X]$, which is used to compute the deformation gradient vector $\{F\}$ in (3.44), is then given by

$$[B_X] = \begin{bmatrix} \Psi_{11} & \Psi_{12} & 0 & 0 \\ 0 & 0 & \Psi_{21} & \Psi_{22} \\ \Psi_{21} & \Psi_{22} & 0 & 0 \\ 0 & 0 & \Psi_{11} & \Psi_{12} \end{bmatrix} [D]. \tag{A.13}$$

The matrix $[B_x]$ is computed similarly to $[B_X]$; this time using the current coordinates $\{x\}$ instead of the reference coordinates $\{X\}$.

To compute the gradients w.r.t. the current coordinates $\boldsymbol{x}$, we require the element Jacobian $\boldsymbol{j}$, which is defined as

$$\boldsymbol{j} = \begin{bmatrix} \frac{dx}{d\xi} & \frac{dy}{d\xi} \\ \frac{dx}{d\eta} & \frac{dy}{d\eta} \end{bmatrix} = \begin{bmatrix} j_{11} & j_{12} \\ j_{21} & j_{22} \end{bmatrix}. \tag{A.14}$$

Application of the chain rule results in

$$\boldsymbol{j} = \boldsymbol{J}\boldsymbol{F}^{\mathrm{T}}. \tag{A.15}$$

The inverse of the Jacobian $\boldsymbol{j}$ is denoted $\boldsymbol{\psi}$, and the matrix $[B_x]$ is given by

$$[B_x] = \begin{bmatrix} \psi_{11} & \psi_{12} & 0 & 0 \\ 0 & 0 & \psi_{21} & \psi_{22} \\ \psi_{21} & \psi_{22} & \psi_{11} & \psi_{12} \end{bmatrix} [D]. \tag{A.16}$$

The derivatives of the matrix $[B_x]$ w.r.t. nodal displacements are given by

$$\frac{d[B_x]}{dU_i} = \begin{bmatrix} \frac{d\psi_{11}}{dU_i} & \frac{d\psi_{12}}{dU_i} & 0 & 0 \\ 0 & 0 & \frac{d\psi_{21}}{dU_i} & \frac{d\psi_{22}}{dU_i} \\ \frac{d\psi_{21}}{dU_i} & \frac{d\psi_{22}}{dU_i} & \frac{d\psi_{11}}{dU_i} & \frac{d\psi_{12}}{dU_i} \end{bmatrix} [D], \tag{A.17}$$

which requires the derivative of the inverse of the Jacobian $\frac{\mathrm{d}\boldsymbol{\psi}}{\mathrm{d}U_i}$. This is computed as

$$\frac{\mathrm{d}\boldsymbol{\psi}}{\mathrm{d}U_i} = \frac{\mathrm{d}\boldsymbol{j}^{-1}}{\mathrm{d}U_i} = -\boldsymbol{j}^{-1}\frac{\mathrm{d}\boldsymbol{j}}{\mathrm{d}U_i}\boldsymbol{j}^{-1}, \tag{A.18}$$

where the derivative of the Jacobian $\boldsymbol{j}$ w.r.t. nodal displacements follows by differentiating (A.15):

$$\frac{\mathrm{d}\boldsymbol{j}}{\mathrm{d}U_i} = \boldsymbol{J}\frac{\mathrm{d}\boldsymbol{F}^{\mathrm{T}}}{\mathrm{d}U_i}. \tag{A.19}$$

The derivative $\frac{d\{F\}}{d\{U_i\}}$ is simply $[B_X]$, which follows directly from (3.44).

Appendix B

Finite element analysis of MEMS using analytical gradient

The derivative of the kinematic matrix $[B_x]$ with respect to the nodal coordinates $\{x\}$ follows exactly the same procedure as described in Appendix A, where the derivative of $[B_x]$ with respect to the displacements $\{U\}$ is detailed.

The derivative of the determation of a matrix $\boldsymbol{A}$ that depends on a scalar x is given by

$$\frac{d\det(\boldsymbol{A}(x))}{dx} = \det(\boldsymbol{A}(x))\text{trace}\left(\frac{d\boldsymbol{A}(x)}{dx}\boldsymbol{A}(x)^{-1}\right). \tag{B.1}$$

This reuslts is required in (4.41) to compute $\frac{\partial \det(\boldsymbol{j})}{\partial\{x_e\}}$.

For linear interpolation along any element edge, the interpolation matrix $\boldsymbol{M}$, required in (4.15), is given by

$$[\boldsymbol{M}] = \frac{L_{element}}{6}\begin{bmatrix} 2 & 0 & 1 & 0 \\ 0 & 2 & 0 & 1 \\ 1 & 0 & 2 & 0 \\ 0 & 1 & 0 & 2 \end{bmatrix}. \tag{B.2}$$